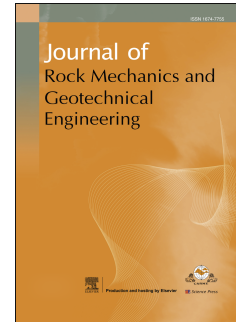


Journal Pre-proof

A hybrid data-driven approach for rainfall-induced landslide susceptibility mapping:
Physically-based probabilistic model with convolutional neural network

Hongzhi Cui, Bin Tong, Tao Wang, Jie Dou, Jian Ji



PII: S1674-7755(24)00355-X

DOI: <https://doi.org/10.1016/j.jrmge.2024.08.005>

Reference: JRMGE 1674

To appear in: *Journal of Rock Mechanics and Geotechnical Engineering*

Received Date: 20 May 2024

Revised Date: 13 July 2024

Accepted Date: 14 August 2024

Please cite this article as: Cui H, Tong B, Wang T, Dou J, Ji J, A hybrid data-driven approach for rainfall-induced landslide susceptibility mapping: Physically-based probabilistic model with convolutional neural network, *Journal of Rock Mechanics and Geotechnical Engineering*, <https://doi.org/10.1016/j.jrmge.2024.08.005>.

This is a PDF file of an article that has undergone enhancements after acceptance, such as the addition of a cover page and metadata, and formatting for readability, but it is not yet the definitive version of record. This version will undergo additional copyediting, typesetting and review before it is published in its final form, but we are providing this version to give early visibility of the article. Please note that, during the production process, errors may be discovered which could affect the content, and all legal disclaimers that apply to the journal pertain.

© 2024 Institute of Rock and Soil Mechanics, Chinese Academy of Sciences. Production and hosting by Elsevier B.V. All rights are reserved, including those for text and data mining, AI training, and similar technologies.

Full length article

A hybrid data-driven approach for rainfall-induced landslide susceptibility mapping: Physically-based probabilistic model with convolutional neural network

Hongzhi Cui ^{a,b}, Bin Tong ^a, Tao Wang ^a, Jie Dou ^c, Jian Ji ^{a,*}^a Key Laboratory of Ministry of Education for Geomechanics and Embankment Engineering, Hohai University, Nanjing, 210024, China^b Division of Geotechnical Engineering and Geosciences, Department of Civil and Environmental Engineering, Universitat Politècnica de Catalunya, Barcelona, 08034, Spain^c Badong National Observation and Research Station of Geohazards, China University of Geosciences, Wuhan, 430074, China

*Corresponding author. E-mail address: jii0003an@e.ntu.edu.sg (Jian Ji)

Abstract: Landslide susceptibility mapping (LSM) plays a crucial role in assessing geological risks. The current LSM techniques face a significant challenge in achieving accurate results due to uncertainties associated with regional-scale geotechnical parameters. To explore rainfall-induced LSM, the study proposes a hybrid model that combines the physically-based probabilistic model (PPM) with convolutional neural network (CNN). The PPM model is capable of effectively capturing the spatial distribution of landslides by incorporating the probability of failure (POF) considering the slope stability mechanism under rainfall conditions. This significantly characterizes the variation of POF caused by parameter uncertainties. CNN is used as a binary classifier to capture the spatial and channel correlation between landslide conditioning factors and the probability of landslide occurrence. OpenCV image enhancement technique is utilized to extract non-landslide points based on the POF of landslides. The proposed model considers physical mechanics comprehensively when selecting non-landslide samples, which can effectively filter out samples that do not adhere to physical principles and reduce the risk of overfitting. The results indicate that the proposed PPM-CNN hybrid model presents a higher prediction accuracy, with an area under the curve (AUC) value of 0.85 based on the landslide case of the Niangniangba area of Gansu Province, China compared with the individual CNN model ($AUC = 0.61$) and the PPM model ($AUC = 0.74$). This model can also consider the statistical correlation and non-normal probability distributions of model parameters. These results offer valuable insights for future research in conducting rainfall-induced landslide susceptibility assessment at the regional scale.

Keywords: Rainfall landslides; Landslide susceptibility mapping; Hybrid model; Physically-based model; Convolution neural network (CNN); Probability of failure (POF)

1. Introduction

Landslides are the globally prevalent geological hazards, often resulting in extensive property damage and even fatalities (Hung et al., 2014; Chen et al., 2023; Mondini et al., 2023; Zhu et al., 2024). However, accurately predicting the potential locations of future landslides remains a significant challenge. Landslide susceptibility mapping (LSM) based on landslide inventories and associated conditioning factors is one of the effective measures to address this issue. It has now been widely used by decision-makers to determine regional distributions of landslide hazards. Currently, two primary LSM categories exist for landslide prediction: physical modeling approaches and data-driven approaches.

Physically-based models are extensively employed in regional landslide susceptibility analysis due to their generic applicability. This approach typically adopts the limit equilibrium slope stability model with external disaster factors (i.e. earthquakes, rainfall) to depict the physical process of landslides (Hess et al., 2017; Cui et al., 2022; Ji et al., 2022; Ye et al., 2024). The widely utilized physically-based models, such as TRIGRS, SINMAP, SHALSTAB, SLIP, and FSLAM (Montgomery and Dietrich, 1994; Pack et al., 1998; Baum et al., 2008; Montrasio et al., 2011; Medina et al., 2021), are frequently employed for regional-scale assessment of landslide susceptibility induced by rainfall. Additionally, several physically-based models based on Green-Ampt (Green and Ampt, 1911) infiltration analysis have subsequently been developed and employed in the investigation of LSM, such as the YS-model (Kim et al., 2014) and SPRIn-SL (Raimondi et al., 2023). However, these models are subjected to several limitations arising from the modeling assumptions, as well as the requirements for extensive and high-quality data. The evaluation of model inputs can only be accomplished through empirical equations or inverse analysis (Catani et al., 2010; Segoni et al., 2012). Also, physically-based models are susceptible to over-prediction, resulting in high false positive rates (Liao et al., 2010).

Recently, the advancement of machine learning (ML) models and their exceptional predictive performance have led to widespread application in regional LSM (Zeng et al., 2024). These ML models encompass logistic regression, support vector machine, and random forest (Kalantar et al., 2018; Liu et al., 2021; Fang et al., 2022; Topaçlı et al., 2024). However, most existing ML algorithms prioritize the analysis of the

impact of different influencing factors. With the rapid advancement of research, it has become evident that conventional ML models are unable to discern the latent relationships within landslide and other natural disaster data, thus impeding further enhancement of prediction accuracy (Wang et al., 2019). To address this problem, a subfield of machine learning (ML) known as deep learning (DL) has emerged as one of the most effective approaches due to its superior capability in addressing the target problem compared to conventional ML methods (Ullah et al., 2022). The convolutional neural network (CNN) exhibits exceptional proficiency in handling imagery data with distinct spatial structures which is regarded as an advanced ML technique. The inherent characteristics of CNN prompt its extensive utilization across various domains in geotechnical or geological engineering (Wang et al., 2021). While CNNs have been widely used in landslide-related research, particularly for landslide identification based on remotely sensed imagery (Anantrasirichai et al., 2019; Lei et al., 2019), their utilization in LSM remains relatively limited by several technical aspects. For instance, a CNN model (Li et al., 2022) has been developed to evaluate landslide susceptibility in the Zigui-Badong section of the Three Gorges region in China, but it neglects the spatial correlation of data by aggregating grids/cells into larger assessment units using a multi-resolution segmentation algorithm. Although CNN models have been commonly used to address factors related to landslides, it is necessary to further explore and improve their ability to identify and utilize spatial data structured in landslide susceptibility assessment.

In contrast to the physically-based modeling approach in landslide prediction, the data-driven approach emphasizes establishing a correlation between landslide conditioning factors and actual landslide inventories (Liu et al., 2023; Huang et al., 2024; Sun et al., 2024). Therefore, the quality of the landslide sample dataset is crucial for accurate LSM using a data-driven approach. The landslide dataset comprises historical landslide points and non-landslide points. With advancements in Earth satellite observation technology, the selection accuracy of historical landslide points (positive samples) has been significantly improved. The selection of non-landslide points (negative samples) with scientific backing becomes equally important as it directly influences the ML model's capability on the other side. The current prevailing approach for selecting non-landslide points involves random sampling within a specified distance from historical landslide occurrences. However, the logic behind this means has not been fully demonstrated. To mitigate the risk of misclassification between positive and negative samples, Wei et al. (2021) proposed a novel method by integrating CNN with TRIGRS to label non-landslide points using a safety factor-based slope stability model. Liu et al (2024) employed the Scoops3D software to extract non-landslide points and construct a landslide sample dataset. The physically-based model approach allows for a comprehensive consideration of physical mechanics underlying the rainfall-induced landslides when selecting non-landslide samples which can effectively filter out samples. This process adheres to physical principles, thereby mitigating the risk of model overfitting.

Although the aforementioned approach combines physically-based and ML models, it primarily relies on deterministic analyses to construct negative samples, disregarding the influence of uncertainty of geotechnical parameters. This inherent limitation inevitably gives rise to disparities in the spatial distribution of LSM when considering the uncertainties associated with geotechnical parameters (Ji et al., 2022; Cui et al., 2023, 2024), which could compromise the quality of selected non-landslide points. One possible way to construct more effective non-landslide points is to integrate the probabilistic analysis to enhance the accuracy of LSM. Unfortunately, there are very few LSM methods successfully integrating the PPM with the ML framework to predict landslides at the regional scale.

In this study, we present an innovative LSM framework that utilizes the results of PPM as one of the input layers for CNN model training. The proposed model demonstrates a significant improvement of the LSM accuracy through a case study of the rainfall-induced landslide area in Niangniangba, Gansu Province, China. The primary objectives of this study are: (1) to propose a hybrid data-driven approach that combines physically-based probabilistic model with CNN (PPM-CNN); (2) to assess the effect of optimizing the output of this novel method using the OpenCV image processing technique; and (3) to explore the influence of geotechnical parameter uncertainties on the LSM at the regional scale by considering different patterns for coefficient of variation (*COV*), cross-correlation, and statistical distribution.

2. Methodology

2.1. Brief description of physically-based modeling: the PRL-STIM model for rainfall-induced landslides

Conducting physically-based probabilistic modeling for rainfall-induced LSM is a challenging task. A recently proposed novel physically-based model called "Physically-based probabilistic modeling of Rainfall Landslide using Simplified Transient Infiltration Model (PRL-STIM)" is adopted in this study (Cui et al., 2024). This model calculated the factor of safety (FOS) by employing the infinite slopes based on limit equilibrium analysis. The wetting front depth (WFD) is considered to simulate the process of rainfall-induced transient infiltration. To describe the variation of WFD (z_w), the model considers unsaturated soil strength with three different pore water pressure (PWP) profiles as outlined by Rahardjo et al. (1995). The three different PWP profiles are illustrated in Fig. 1, and can be formulated as follows (Huang et al., 2022):

$$u_w(z) = \begin{cases} -\frac{z}{z_w} \gamma_w h_c & \text{(for Profile a)} \\ 0 & \text{(for Profile b)} \\ \gamma_w z (\cos \beta)^2 & \text{(for Profile c)} \end{cases} \quad (1)$$

where

$$h_c = (H - z_w) \cos^2 \beta$$

where u_w denotes the PWP at a vertical depth of z ($0 \leq z \leq z_w$), γ_w is the unit weight of water, h_c the initial suction head at $z = z_w$ before rainfall infiltration, and β denotes the slope angle.

The limit equilibrium-based FOS is given by

$$FOS = \frac{c'_s}{\gamma_{\text{sat}} z_w \sin \beta \cos \beta} + \frac{\tan \phi'}{\tan \beta} - \frac{\chi u_w}{\gamma_{\text{sat}} z_w \sin \beta \cos \beta} \quad (2)$$

where γ_{sat} denotes the saturated unit weight of soil, and c'_s and ϕ' denotes soil effective cohesion.

Note that Eq. (2) is the general expression of FOS for the PWP profiles shown in Fig. 1, and u_w is calculated by Eq. (1) with $z = z_w$. The effective stress parameter $\chi = 1$ is adopted for saturated soil slopes (Huang et al., 2022).

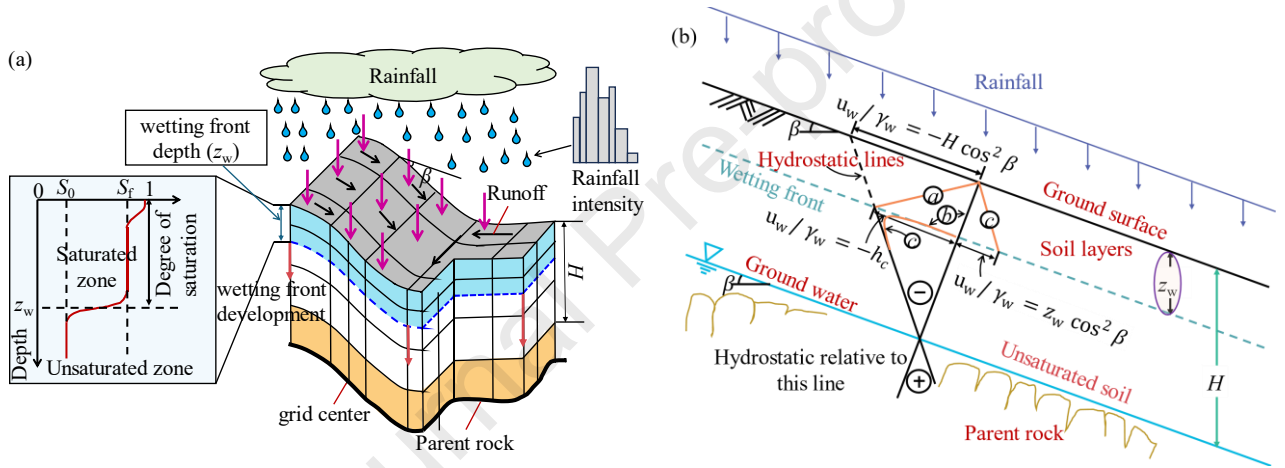


Fig. 1. PRL-STIM modeling: (a) Conceptual schematic, and (b) rainfall-infiltration infinite slope stability model incorporating unsaturated soils and three PWP profiles: Profiles a, b, and c (adapted from Rahardjo et al. (1995)).

For the implementation of PRL-STIM, several necessary parameters need to be further calculated. Firstly, in the case of rainfall intensity I_R , which changes with time, z_w is evaluated by the following expression (Lumb, 1962; Sun et al., 1998; Zhang et al., 2011):

$$z_w = \begin{cases} \frac{k_s t}{n(S_f - S_o)} \\ \frac{I_R t}{n(S_f - S_o)} \end{cases} \quad (3)$$

$$z_{wti} = z_{wt(i-1)} + \Delta z_{wti} \quad (4)$$

where

$$\left. \begin{aligned} S_f &= \frac{\theta_s}{n} \\ S_o &= \frac{\theta_o}{n} \end{aligned} \right\} \quad (5)$$

where z_{wti} denotes the WFD at t_i ; Δz_{wti} denotes the increased WFD at t_i ; k_s is the saturated coefficient of permeability; n is the soil porosity; S_f is the final degree of saturation; S_o is the initial degree of saturation; θ_o , θ_s are the initial and final volumetric water content, respectively.

Meantime, the Δz_{wti} can be rewritten by introducing a component of $\cos \beta$ (Lee et al., 2009):

$$\Delta z_{wi} = \begin{cases} \frac{k_s \Delta t}{(\theta_s - \theta_0) \cos \beta} & (I_R \geq k_s) \\ \frac{I_R \Delta t}{(\theta_s - \theta_0) \cos \beta} & (I_R < k_s) \end{cases} \quad (6)$$

Note that the wetting front depth, z_{wfi} , is controlled by the entire depth of the soil (h_s), we have

$$z_{wfi} = \begin{cases} h_s & (z_{wfi} \geq h_s) \\ z_{wfi} & (z_{wfi} < h_s) \end{cases} \quad (7)$$

Additionally, the infiltration I_R is calculated at each cell as the sum of the precipitation (P) and any upslope cell runoff (R_u), subjected to the constraint that it must not exceed the saturated hydraulic conductivity (k_s):

$$I_R = \begin{cases} P + R_u & (P + R_u < k_s) \\ k_s & (P + R_u \geq k_s) \end{cases} \quad (8)$$

At each cell where $P + R_u \geq k_s$, the excess is considered the runoff R_d , and it is diverted to adjacent downslope cells:

$$R_d = \begin{cases} P + R_u - k_s & (P + R_u - k_s \geq 0) \\ k_s & (P + R_u - k_s > 0) \end{cases} \quad (9)$$

The final infiltration I , which is different from the rainfall intensity I_R , can be calculated by considering the saturated hydraulic conductivity as follows:

$$I = \begin{cases} k_s & (I_R \geq k_s) \\ I_R & (I_R < k_s) \end{cases} \quad (10)$$

It should also be noted that determination of the potential soil thickness is a fundamental variable, as it plays a critical role in many tasks for shallow landslide analysis at the regional scale (Segoni et al., 2012). The Z-model is widely recognized as a simplistic approach and has been also extensively utilized in numerous studies to ascertain the soil thickness (Hwang et al., 2023) as follows:

$$Z_{\text{model}} : h_i = h_{\max} - \frac{Z_i - Z_{\min}}{Z_{\max} - Z_{\min}} (h_{\max} - h_{\min}) \quad (11)$$

where h_{\max} and h_{\min} are the maximum and minimum soil thickness, respectively; h_i denotes the soil depth of each cell; Z_i is the elevation of each cell, and Z_{\max} and Z_{\min} are the maximum and minimum elevation, respectively.

2.2. Fast computational technique for landslide probability analysis: the FORM with HLRF-x recursive algorithm

The computation of FOS using Eq. (2) is very fast, thus making it possible for regional landslide prediction. However, the model input parameters are by no means deterministically available at a regional scale. To account for these uncertain input parameters, the physically-based model in terms of FOS can be mathematically extended into the probabilistic description, such that

$$\left. \begin{aligned} P_f &= \int_{g(\mathbf{x}) < 0} f(\mathbf{x}) d\mathbf{x} \\ g(\mathbf{x}) &= FOS(\mathbf{x}) - 1 \end{aligned} \right\} \quad (12)$$

where P_f is the probability of failure (POF), the vector $\mathbf{x} = \{c_s, \tan \phi, \beta, n, \gamma_{\text{sat}}, \dots\}$ denotes a collection of random variables (of input parameters), $f(\mathbf{x})$ is the joint probability distribution function of random variables \mathbf{x} , and $FOS(\mathbf{x})$ is a functional format of Eq. (2). It is noted that the second line of Eq. (12) is the limit state function (LSF).

This integral equation for P_f is almost impossible to solve at speed, not to mention for regional landslide analysis. Alternatively, an efficient approximate solution known as the first order reliability method (FORM) can be adopted, which has the following necessary recipes:

$$P_f = \Phi(-\beta_f) \quad (13)$$

$$\beta_f = \sqrt{\left(\frac{\mathbf{x}_i^* - \mathbf{u}_i^N}{\sigma_i^N} \right)^T \mathbf{R}^{-1} \left(\frac{\mathbf{x}_i^* - \mathbf{u}_i^N}{\sigma_i^N} \right)} \quad (14)$$

where $\Phi(\cdot)$ denotes the standard normal cumulative distribution function; β_f is the reliability index, \mathbf{x}_i^* denotes the most probable failure point

(MPP) value of i th random variable; μ_i^N and σ_i^N denote the equivalent normal mean and standard deviation of the i th variable, respectively, and they contain important information of \mathbf{x} semi-probability distribution functions; and \mathbf{R} is the correlation matrix. A detailed explanation can be found in Low and Tang (2007).

FORM is a semi-probability calculation method that is well-known in geotechnical engineering failure analysis. The fundamental concept of the FORM probabilistic calculation is to find the reliability index (RI , or β_I) evaluated at the MPP. In this work, we adopt the fast recursive algorithm HLRF- \mathbf{x} proposed by Ji et al. (2015; 2019) to implement the FORM calculation into GIS. In brief, the HLRF- \mathbf{x} recursive algorithm for locating the MPP in the space of physical random variables defined by vector \mathbf{x} (\mathbf{x} -space) is written as follows:

$$\left. \begin{aligned} \mathbf{x}_{k+1} &= \mu_k^N + \frac{1}{\nabla g(\mathbf{x}_k)^T \mathbf{T}_k \nabla g(\mathbf{x}_k)} [\nabla g(\mathbf{x}_k)^T (\mathbf{x}_k - \mu_k^N) - g(\mathbf{x}_k)] \mathbf{T}_k \nabla g(\mathbf{x}_k) \\ \mathbf{T}_k &= [\sigma_k^N]^T \mathbf{R} [\sigma_k^N] \end{aligned} \right\} \quad (15)$$

where \mathbf{T}_k is the transformation matrix, \mathbf{x}_k is the vector of random variables in \mathbf{x} -space, μ_k^N is the vector of equivalent MV to convert random variables into the normal distribution, and $\nabla g(\mathbf{x}_k)$ denotes the gradient vectors of the LSF evaluated at \mathbf{x}_k .

Further, for the diagonal matrix $\begin{bmatrix} \sigma_{k,i}^N & \cdots & 0 \\ \vdots & \sigma_{k,n}^N & \vdots \\ 0 & \cdots & \sigma_{k,m}^N \end{bmatrix}$, $\sigma_{k,i}^N$ is the equivalent normal standard deviation of the i th random variables evaluated

at \mathbf{x}_k .

2.3. OpenCV

When a computational data result is compiled into an image, isolated noisy points (i.e. separate cells) will inevitably appear in the generated LSMs. These noisy cells may affect the LSM prediction results, especially when constructing samples for random sampling of non-landslide points (Wei et al., 2021). Removing noise from images while preserving their main morphological structure is a challenging task. The efficient image processing techniques can be used to optimize and cluster the resulting raster. However, there has been limited research conducted in this aspect. Note that the OpenCV (Open Source Computer Vision Library) is a widely used open-source software library for computer vision which plays a crucial role in image processing, video analysis, visual perception, and the development of complex visual systems (Zhang et al., 2023). The OpenCV technique has been widely used in various fields, especially in text recognition and biomedical image analysis. In this study, we will explore the possibility of using this technique in LSM. The diverse image filtering algorithms offered by OpenCV, including Gaussian and median filtering, can effectively diminish noise and outliers in the LSM, eradicate local irregularities, and render the LSM more uniform and continuous. Morphological operations, such as dilation and erosion, can be employed to modify the shape and size of high-risk areas within the LSM, while simultaneously eliminating isolated small areas. This results in a more continuous and realistic representation of the risk areas. Moreover, the histogram equalization technology provided by OpenCV can enhance contrast within the LSM, facilitating differentiation between various risk levels. It is noteworthy that OpenCV enables precise pixel-level manipulations on the LSM for fine-tuning and calibration based on specific requirements. Through these processing steps, OpenCV significantly enhances the visual quality, interpretability, and practicality of the LSM while concurrently improving overall accuracy and reliability.

The conceptual operations involved in OpenCV can be summarized in the following main steps as shown in Fig. 2a-f:

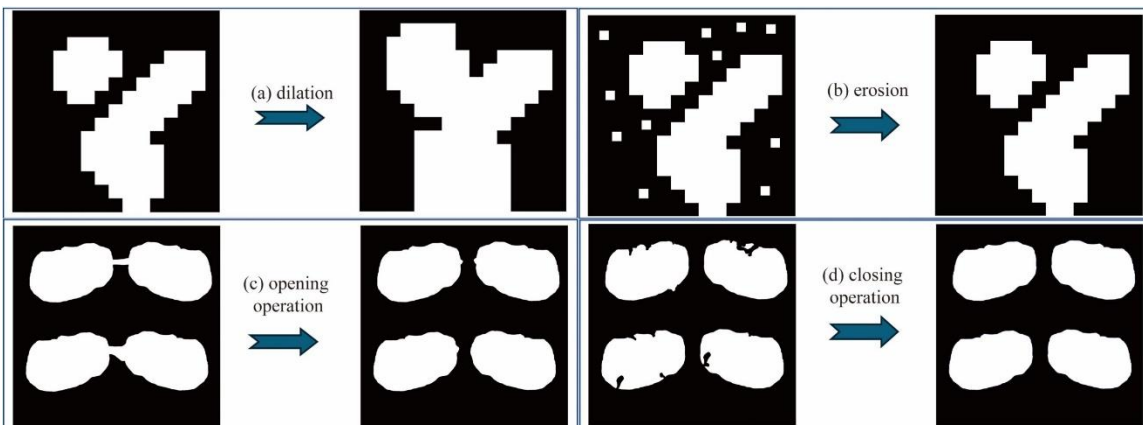


Fig. 2. Basic morphological operation (adapted from Raid et al., (2014)).

(1) Dilation

$$\text{Dilation}(A,B) = \{z | (\hat{B}_z \cap A) \neq \emptyset\} \quad (16)$$

(2) Erosion

$$\text{Erosion}(A,B) = \{z | B_z \subseteq A\} \quad (17)$$

(3) Opening operation

$$\text{Opening}(A) = \text{Dilation}[\text{Erosion}(A,B),B] \quad (18)$$

(4) Closing operation

$$\text{Closing}(A) = \text{Erosion}[\text{Dilation}(A,B),B] \quad (19)$$

where A typically represents the original or processed image, namely, a set in which each pixel is considered an element of the set in morphological operations; and B usually stands for a structuring element, which is a tool used to detect a specific shape or pattern in image A . The structuring element can be of any shape and size, but simple shapes such as circles, squares or crosses are usually chosen.

2.4. Convolution neural network (CNN)

The convolutional neural network (CNN) has gained widespread recognition and application in the field of geotechnical engineering, as documented in the literature (Sameen et al., 2020; Wang, 2022). This approach has demonstrated significant efficiency in addressing LSM by incorporating various landslide conditioning factors such as terrain slope, aspect, elevation, vegetation distribution, and data from actual landslide occurrences. Those different landslide conditioning factors shown in different digital images can be analogized as distinct "channels" to the CNN model, each of which effectively constructs an "image" that characterizes both the spatial distribution and intensity levels indicative of landslide susceptibility.

The CNN model in this paper consists of several layers, including an input layer, a convolutional layer, a maximum pooling layer, a fully connected layer and an output layer, as shown in Fig. 3. Firstly, the input layer plays a crucial role in normalizing the input image, which is characterized by its dimensions of height, width, and number of channels. In this case, the size of the input layer for the baseline model is $17 \times 17 \times 6$, with 6 channels specifically representing the landslide conditioning factors. Subsequently, the image undergoes feature extraction through multiple filters in the convolutional layer. Our model is composed of three convolutional layers, with channel numbers and filter sizes determined by Bayesian optimization. After each convolutional layer, the activation function ReLU (Rectified Linear Unit) is applied to non-linearly map the output, followed by a BN (Batch Normalization) layer for accelerating model training and mitigating overfitting issues.

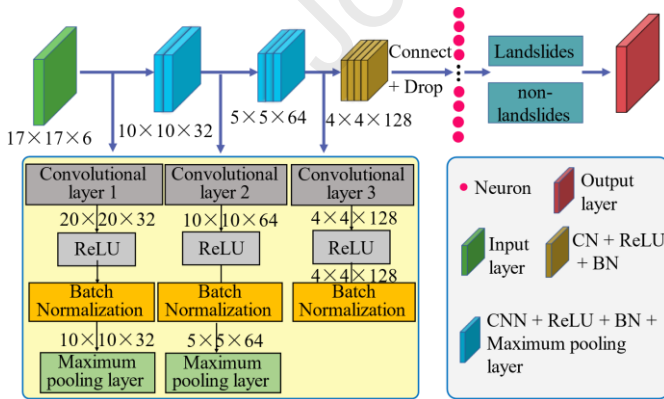


Fig. 3. CNN architecture used in the present study.

After the initial two BN layers, a maximum 2×2 pooling layer with a stride of 1 is employed to extract relevant information for outcome discrimination. Subsequently, a fully connected layer is utilized to transform the 2D feature mapping into 1D data for classification or regression purposes. This layer is added after the final BN layer, and an additional dropout layer is introduced to mitigate overfitting, resulting in the retention of precisely 304 neurons. The output layer employs two neural units to represent landslides and non-landslides, respectively. It generates landslide susceptibility values for each raster point, thereby producing the entire LSM for the study area.

To optimize the CNN model performance, it is essential to perform hyperparameter adjustment. The common methods for hyperparameter optimization include grid search (Liu et al., 2024), random grid search, and Bayesian optimization (Balogun et al., 2021). The Bayesian

optimization exhibits superior efficiency by incorporating prior parameter information through the integration of prior knowledge with a Gaussian process and continuously updating the assumptions during iterations. As listed in Table 1, the optimization ranges, default values, and optimal parameters after optimization for these hyperparameters are presented by implementing the Bayesian method. Fig. 4 demonstrates the relationship between the number of Bayesian optimizations. The results demonstrate that with an increasing number of optimizations, the accuracy exhibits a continuous improvement until it reaches a stable level. Meanwhile, the loss consistently decreases and eventually converges.

Table 1

The CNN hyperparameters for Bayesian optimization.

Hyperparameter	Optimization interval	Default	Best parameters
Convolution kernel size	[2, 3, 4, 5]	3	3
Initial learning rate	$[1 \times 10^{-5}, 1 \times 10^{-1}]$	0.01	5.6×10^{-3}
L2 regularization factor	$[1 \times 10^{-6}, 1 \times 10^{-2}]$	0.01	0.1
Dropout rate	[0, 0.5]	0.2	0
Channel	[32, 64, 128]	32	64

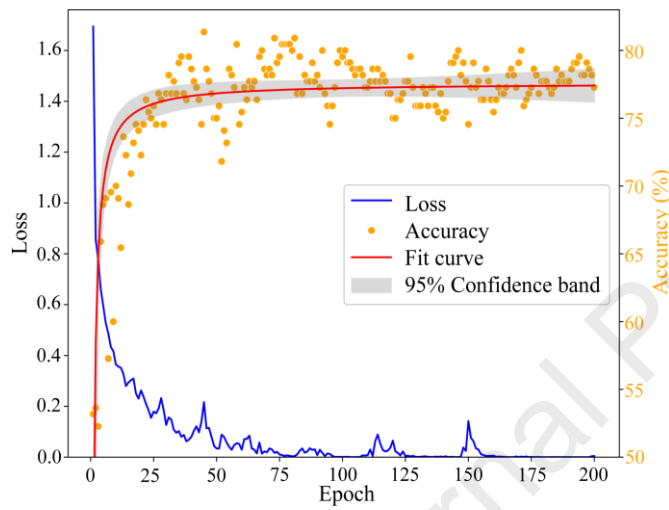


Fig. 4. The convergence of the CNN training process combining Bayesian optimization.

2.5. Methodology and procedures for implementation

Recent studies (Hong et al., 2019; Yang et al., 2024) have demonstrated that the inclusion of non-landslide samples introduces uncertainty that significantly impacts the accuracy of landslide prediction. In contrast to conventional methods, the physically-based model approach allows for a comprehensive consideration of the physical mechanics underlying rainfall-induced landslides when selecting non-landslide samples. This approach effectively filters out samples that do not adhere to physical principles, thereby mitigating the risk of model overfitting. However, this method poses challenges in fully addressing the uncertainty of geotechnical parameters at the regional scale.

Considering this, a hybrid model that integrates the PPM with the CNN method is innovatively integrated to address this phenomenon in this study. The predicted outcomes from the PPM are utilized as input information for the CNN. This means that this method does not involve the screening of conditioning factors (or feature selection) which is different from a traditional ML-based landslide susceptibility assessment. The morphological operations (utilizing the open-source computer vision library, OpenCV) are employed to optimize the processing of raster images. This method will obtain a more precise landslide susceptibility mapping under transient rainfall conditions while accounting for uncertainties in physical parameters. The process of implementing the proposed PPM-CNN coupling framework to address regional rainfall-induced shallow landslides can be delineated into the following six steps, and the key elements are visually illustrated in Fig. 5:

- (1) Step 1. Input the necessary PPM dataset, which includes topography, geological information, geotechnical and hydraulic parameters, as well as their statistical and rainfall data for simulating rainfall conditions.
- (2) Step 2. Utilize PRL_STIM v1.0 software to read the prepared dataset and perform runoff calculations along with slope stability calculations under hydrological conditions. This will yield the FOS, which can be further used in batch calculations of POF using HLRF_x software to predict regional shallow landslide susceptibility based on the physical model.
- (3) Step 3. Upon completion of the physically-based model calculation, apart from extracting FOS and POF values, it is also essential to

obtain geo-environmental factor datasets (i.e. slope, aspect, and elevation) related to inputs used in the physically-based model calculation in raster layer format as depicted in Fig. 5c. Note that all feature layers are normalized for accelerating convergence, preventing gradient vanishing or exploding, improving model performance, and eliminating input scale differences.

- (4) Step 4. To construct a suitable landslide dataset, the stable area based on POF prediction is randomly selected within the non-landslide region. The original POF layer (Fig. 5e) is initially binarized (Fig. 5d), followed by image enhancement and noise removal using OpenCV for data preprocessing. Simultaneously, feature extraction is applied to the parameter dataset (Fig. 5c) used in the physical model.
- (5) Step 5. The prepared input-output data pairs are utilized for training in the designed Bayesian optimized CNN architecture (see Fig. 3). Seventy percent of the dataset is allocated for training purposes, while thirty percent serves as validation data. After sufficient training, the CNN can learn and establish a mapping relationship between inputs and outputs, thereby generating a landslide susceptibility map.
- (6) Step 6. Finally, post-processing techniques involving image enhancement and noise removal using OpenCV are applied once again to refine for more accurate results from the generated LSM obtained in Step 5. This step plays a crucial role in improving CNN's performance through enhanced accuracy during training.

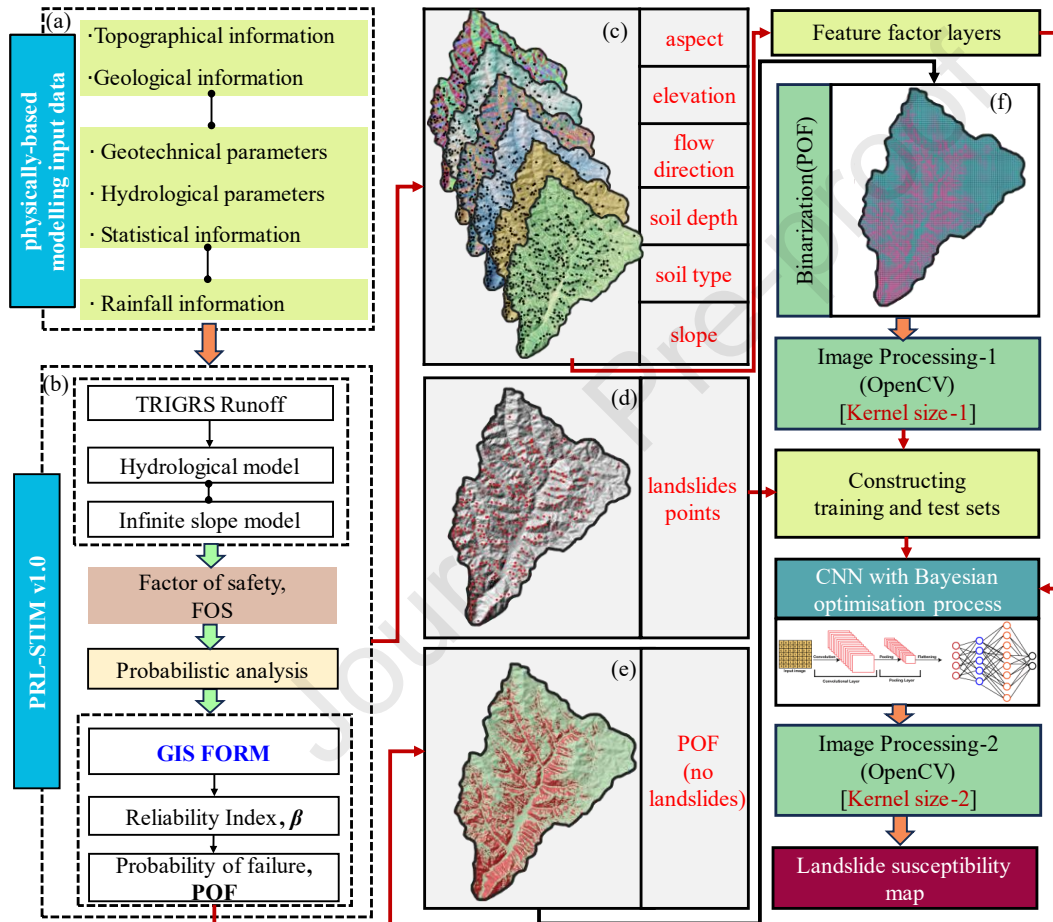


Fig. 5. Implementation procedure of this study.

2.6. Evaluation of model performance and indices of sensitivity analysis

The evaluation of model performance analysis is performed by introducing the receiver operating characteristic (ROC) curve as well as the corresponding area under the ROC curve (AUC) (Cui et al., 2024). This metric provides a comprehensive analysis of model accuracy by considering the true positive rate (TPR) and false positive rate (FPR), as described in Eqs. (20) and (21). The resulting value ranges from 0 to 1, with a higher value signifying enhanced model performance.

$$TPR = \frac{TP}{TP + FN} \quad (20)$$

$$FPR = \frac{FP}{FP + TN} \quad (21)$$

where TP represents the number of true positives and FN represents the number of false negatives. FP is the number of false positives and TN is

the number of true negatives.

Additionally, to evaluate the sensitivity of input parameters for the proposed method, both correlation matrix heatmap and SHAP (SHapley Additive exPlanations) value (Mangalathu et al., 2020) methods are utilized. It should be noted that SHAP values are based on the concept of Shapley value in cooperative game theory which offers a quantitative explanation for the predictive contribution of each feature in a model. The fundamental concept underlying this index is to quantify the fluctuation in model predictions when a feature is incorporated or omitted for accurately evaluating the impact of each feature on the predictive power of the model. The SHAP values enable a thorough comprehension and explanation of the decision-making process of the model, thus significantly improving the transparency and interpretability of the model predictions.

3. Study area and landslide inventory dataset

3.1. Description of the study area

The study area in Niangniangba Town is situated in the southern foothills of the western Qinling mountains, Gansu Province, China. It is characterized by rugged terrain with complex valleys and mountains. The small basin in the northeastern of Niangniangba Town serves as the focal point study, as illustrated in Fig. 6, based on a relative literature report (He et al., 2021). This basin covers an area of 53.81 km² and the elevation ranges from 1416 m asl (above sea level) and 2138 m asl, with an average elevation of 1777 m asl.

The surface layer consists of Quaternary strata with a complex origin, including both landslide accumulation layer (Q4^{del}) and diluvial layer (Q4^{pal}) deposits. The Q4^{pal} strata are confined to the residual valley terrace and have a loose structure and low density, rendering them susceptible to triggering new landslides during periods of rainfall. The soil layer is relatively thin and underlain by various rock strata including Pleistocene Malan loess, Neogene mudstone and sandstone, Anshan period granite, Upper Devonian slate, and quartz sandstone (He et al., 2021). This geological composition increases the susceptibility of this study area to new landslides during rainfall.

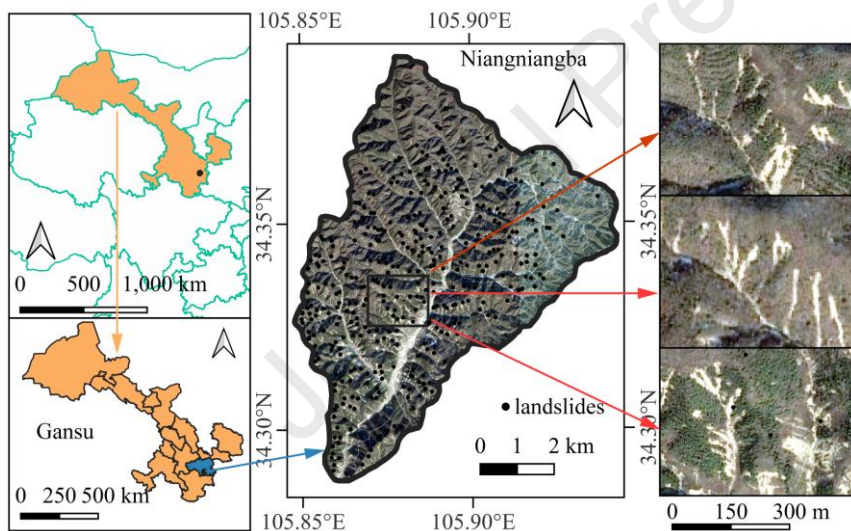


Fig. 6. The Niangniangba study area.

This study area is featured with a temperate continental climate with an average annual relative humidity of 66% and an average annual precipitation of 500.7 mm (1981-2010). Historical data show that 85% of the annual precipitation falls between April and October which indicates a highly heterogeneous distribution. Specifically, the period from July to September experiences the most concentrated precipitation, contributing 68% of the annual total. Consequently, heavy rainfall is identified as the primary factor in triggering geological disasters in this study area. In the month preceding the landslide event, the study area has undergone four heavy rainfall events, which is triple the average for that period. Notably, the cumulative rainfall from 21 to 23 July amounted to 104.3 mm. The rainfall caused catastrophic geological hazards, primarily by shallow landslides according to the reported by He et al. (2021). These landslides are classified as sedimentary soil landslides and typically occur on riverbanks, steep slopes with efficient water catchment conditions, or loess-covered slopes. They are composed of weathered rocks and gravelly soils, with a thickness generally not exceeding 3 meters.

3.2. The 2013 landslides episode

The catastrophic geological hazards resulting from this rainfall primarily consist of shallow landslides characterized by a mixture of weathered rock and gravelly soil on a small scale (He et al., 2021). The clustering pattern of landslides shown in Fig. 1c is evident following the

occurrence of rainfall events. Notably, the orientation of the underlying mudstones aligns with the slope aspect. Composed of weathered rocks and gravelly soil, these landslides typically have a thickness less than 3 m and exhibit significant regional and clustering characteristics. It was reported that the rainfall is concentrated between 12:00 pm on 21 July and 6:00 am on 22 July as shown in Fig. 7. During this period, there is an increase of risk of widespread geological hazards. According to the latest research by Cui et al. (2024), it is asserted that the most extensive occurrence of landslides is associated with a duration of 9 h of rainfall, namely at 21:00. Therefore, the results of shallow landslide susceptibility triggered by rainfall at present (21:00 on 21 July) will be investigated using the proposed hybrid model. The results of the landslide susceptibility map will depict the spatial distribution of landslide risk as predicted by the methodology proposed in this study. In other words, it illustrates the risk ranks of landslides occurring in the Niangniangba area under the influence of this rainfall event.

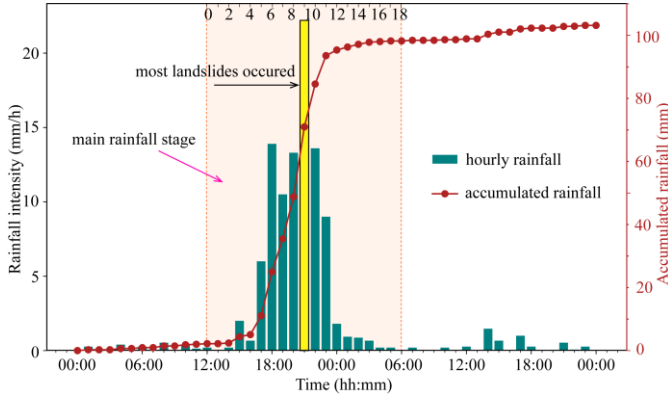


Fig. 7. Rainfall conditions during the July 2013 episode.

3.3. Data preparation

As a physically-based modeling technique, the PRL-STIM model requires three main types of input parameters: topographic parameters (elevation, slope angle, and flow direction) derived from the digital elevation model (DEM), geotechnical parameters, and rainfall information as mentioned in He et al. (2021). Note that input raster files are generated from the DEM. The model utilizes a 12.5 m resolution DEM downloaded from ALOS PALSAR (<https://search.asf.alaska.edu>) before the rainfall event. Additionally, PRL-STIM needs the data of the distribution of slope, flow direction, and soil thickness. The original DEM data are processed to ensure that all topographical areas in the study zone consist of slopes. This process is automatically performed by the PRL-STIM v1.0 software. The single-flow D8 algorithm, employed in PRL-STIM, determines the flow direction of the cell grid, completing the data pre-treatment. Landslides in the study area are characterized by a mix of weathered rock and gravelly soil on a small scale. Soil classification is treated as a single class, as depicted in Fig. 6. The correspondingly typical soil thickness ranges from 0.1 m to 3.0 m. It is worth noting that to ensure compatibility with the DEM, all raster layers utilized must have a resolution of 12.5 m.

Table 2 lists the model parameters including the soil porosity (n), the unit weight of saturated soil (γ_{sat}) and saturated coefficient of permeability (k_s). The rainfall intensity (I_R) is shown in Fig. 7. It should be noted that the initial and final degrees of saturation (S_o , S_f) can be calculated based on the initial and final volumetric water content, as indicated by He et al. (2021).

Table 2

Adopted values of model parameters

Soil class	Parameters	Unit	Distribution	COV	Mean (μ)	Standard deviation
Drab soil and brunisolic soil	c_s	kN/m ²	Normal	0.01, 0.10, 0.20, 0.30	18.5	$\sigma = \mu \cdot COV$
	ϕ	°			20	
	n				0.12	
	S_f				1	
	S_o				0.67	
	γ_{sat}	kg/m ³			25	
	k_s	m/s			2.5×10^{-5}	
	h_s	m	h_{st}			

Note: COV is the coefficient of variation; h_{st} : mean of h_s is assumed to be the value obtained from the soil depth model calculation.

4. Results and discussion

4.1. Parameter sensitivity analysis of the OpenCV-CNN structure

Fig. 8a shows the influence of different parameters in the OpenCV-CNN structure on the SHAP values of AUC which serves to quantify the feature influences for the model's output. The point distribution reveals that threshold, kernel size open, and kernel size exert both positive and negative effects. Among these factors, the points representing the threshold exhibit greater dispersion on either side of the zero line, indicating its most significant impact on model prediction followed by kernel size close. Conversely, although the points corresponding to kernel size open are primarily concentrated near the zero line, they demonstrate a relatively uniform distribution suggesting a comparatively minor influence on model output.

To provide a more precise quantification of the impact of structural parameters on the accuracy (AUC) of our model predictions, we analyzed correlation coefficient plots. As depicted in Fig. 8, there exists a moderate negative correlation (-0.3469) between the threshold and AUC. This suggests that as the threshold increases, there is a tendency for AUC values to decrease. Conversely, we observed a weak negative correlation (-0.1240) between kernel size open and AUC. In contrast to this weaker relationship, the correlation coefficient between kernel size close and AUC was found to be -0.3536, similar to that observed for thresholds, indicating another moderate negative correlation. These findings imply that increasing the value of kernel size close may result in a reduction in AUC comparable to that caused by adjusting thresholds.

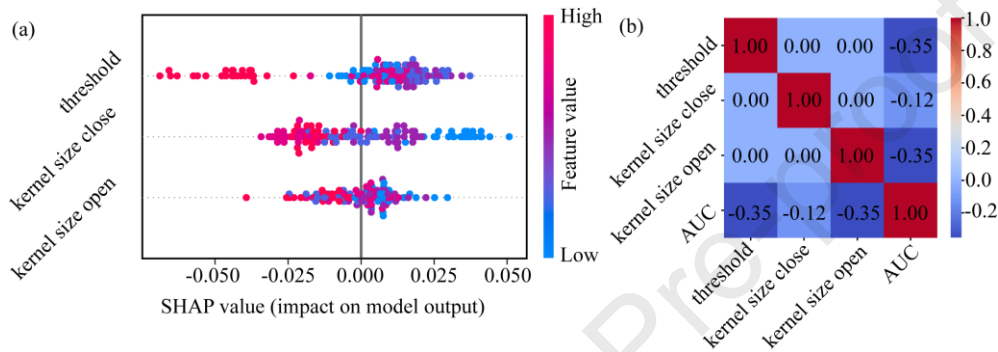


Fig. 8. The sensitivity of three parameters related to the OpenCV-CNN structure: (a) the colors range from blue to red, indicating feature values from low to high. The scatter plot shows the size of the SHAP values on the model output; (b) colors range from blue to red, indicating correlation from negative to positive, with deeper colors showing stronger correlation.

4.2. Comparison of CNN, PPM, PPM-CNN

The LSM results of three different modeling approaches are presented in Fig. 9, including the CNN, PPM (Physically-based probabilistic model PRL-STIM (POF)), and PPM-CNN. When applying the CNN model, using the same set of landslide conditioning factors as that used by the PPM (i.e. slope, aspect, elevation, flow direction, soil depth and soil type shown in Fig. 5c) results in more unstable areas being predicted (Fig. 9a). This indicates that unstable areas (landslides) may be misclassified as stable, leading to an increase in false negative (FN). Conversely, landslide susceptibility assessment using only PPM showed more non-landslide points classified as very hazardous areas, i.e. an increase in False Positive (FP) errors (Fig. 9b). However, when combining PPM with CNN (Fig. 9c), the predicted locations of actual landslides and non-landslides are more accurate and fall within unstable and very stable regions respectively.

To quantitatively evaluate the performance of different models, this study employed ROC curves and their corresponding area under the curve (AUC) to demonstrate the results. Fig. 10 presents a detailed comparison of five different models, namely CNN, PPM, PPM-CNN(N), PPM-CNN(Y1), and PPM-CNN(Y2). Correspondingly, the AUC values for them were found to be 0.61, 0.74, 0.83, 0.85, and 0.67 respectively. The results indicate that the traditional models fall short of the PPM-CNN hybrid models, particularly when combined with OpenCV processing. However, it is also worth noting that the hybrid model (PPM-CNN) performance shows varying degrees of accuracy depending on whether OpenCV is used and the binary threshold selection. Specifically, applying a binary threshold of 0.5 and incorporating OpenCV resulted in the highest AUC value (0.85) for the PPM-CNN (Y1) model. Setting a higher threshold at 0.9 led to poorer performance for PPM-CNN(Y2), with an AUC value of 0.67 due to increased false-negative results. The combination of OpenCV significantly enhances model performance as demonstrated by an AUC value of 0.83 for PPM-CNN(N) without using OpenCV. The POF threshold of 0.5 is considered a significant threshold for regional probabilistic landslide susceptibility assessment in this study. This value has also been adopted in other relevant literature (Silva et al., 2008; Medina et al., 2021; Cui et al., 2024).

Note that the 0.61 of AUC value is obtained when only adopting the CNN method in this study which falls short of expectations. This outcome can be attributed to two primary factors. Firstly, it excludes potentially crucial non-terrain influences. In other words, the absence of data cleaning and feature selection led to inclusion of numerous redundant or irrelevant features, consequently impacting the model's performance. Since the

core of this method involves leveraging parameter information utilized in the PPM as source input data for the CNN model, the condition features used are solely related to PPMs, including slope, aspect, elevation, flow direction, soil layer thickness, and soil type. Furthermore, during the selection of non-landslide points, random sampling was confined to areas outside landslide zones without considering additional information, thereby introducing noise into the data and diminishing the predictive capacity of the model.

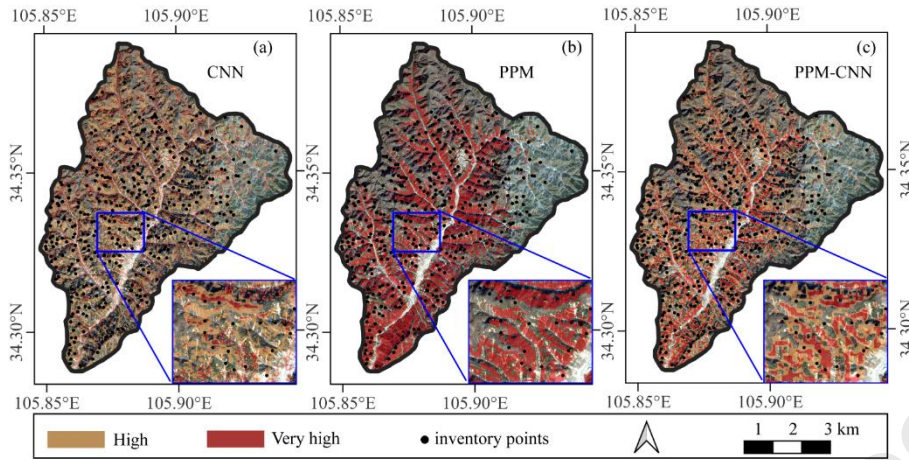


Fig. 9. Landslide susceptibility mapping based on: (a) CNN, (b) PPM, and (c) PPM-CNN.

In contrast, $AUC = 0.85$ was obtained when using the proposed PPM-CNN method following optimization by OpenCV. This approach eschews the traditional feature of selection processes in favor of utilizing the same factors as input and mapping basis for deep learning as employed in the physical model. Therefore, more rational and pertinent non-landslide points by considering the physical mechanisms of landslides are identified to enhance the robustness and accuracy of the model. Furthermore, the probabilistic evaluation method offers supplementary information support for selecting non-landslide points, effectively mitigating issues arising from completely random selection.

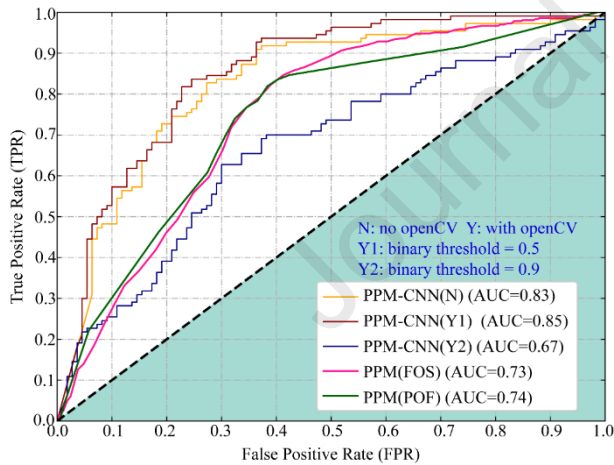


Fig. 10. Receiver operating characteristic (ROC) curves for landslide susceptibility models.

4.3. Influence of different COV scenarios on the proposed method (PPM-CNN)

4.3.1. Comparison analysis of different COV scenarios

For geotechnical parameters on a regional scale, the presence of uncertainty becomes an inevitable concern. In the field of engineering risk analysis, the COV is frequently employed to characterize this phenomenon. The LSMs were obtained by accounting for various COV values ($COV = 0.01, 0.1, 0.2, 0.3$) based on the natural breaks (Jenks) method by using ArcGIS 10.6 software (Merghadi et al. (2020)).

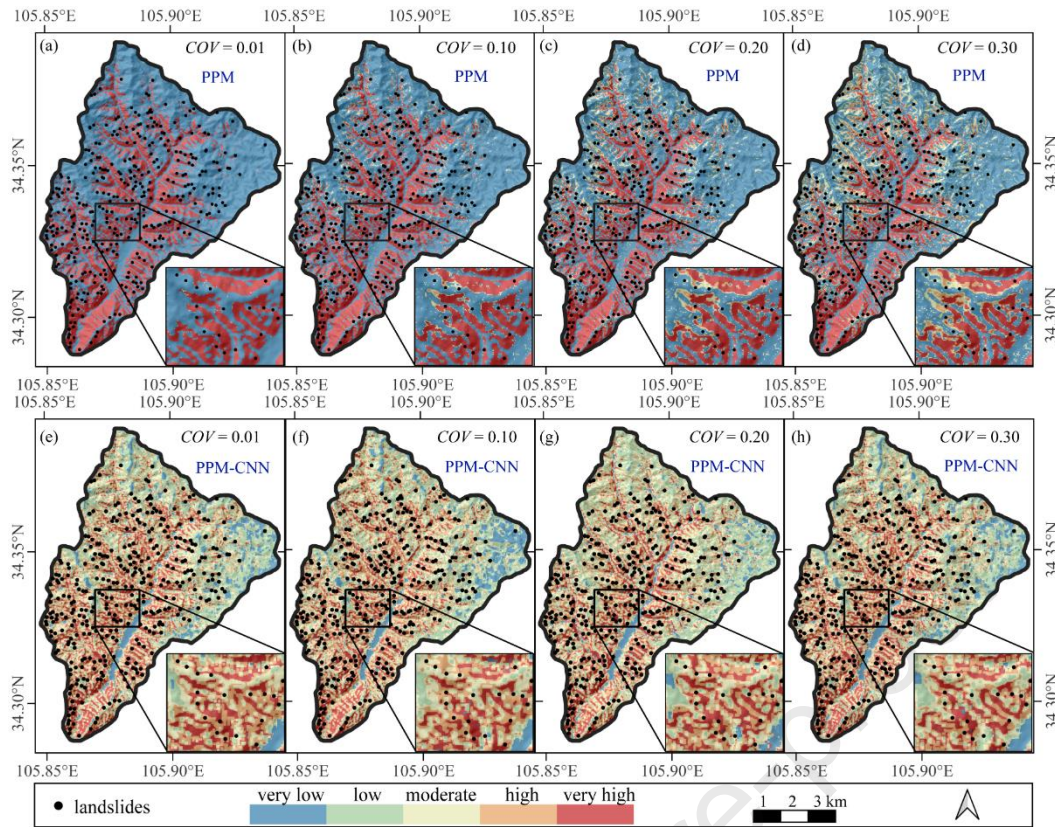


Fig. 11. Landslide susceptible distribution under different $COVs$. PPM: $COV =$ (a) 0.01, (b) 0.10, (c) 0.20, and (d) 0.30; and PPM-CNN: $COV =$ (e) 0.01, (f) 0.10, (g) 0.20, and (h) 0.30.

As shown in Fig. 11a-d, the areas of high susceptibility in the LSM calculated using PPM increase significantly as the COV increases. This variation is more obvious near the inventory landslides. Most of the non-landslide areas were observed located in very low susceptibility levels for PPM-based LSM. However, these areas with non-landslide areas tend to be low and mediate susceptibility levels after adopting PPM-CNN (see Fig. 11e-h). This also demonstrates the capability of the PPM-CNN approach to conduct a more comprehensive analysis of the spatial distribution correlation among parameters by incorporating homologous information, specifically utilizing parameter layers as input features for the CNN within the PPM.

Table 3

FR among the landslide susceptibility classes for different $COVs$.

Methods	Susceptibility grade	Percentage of landslide numbers (%)				Percentage of graded areas (%)				Frequency ratio			
		0.01	0.1	0.2	0.3	0.01	0.1	0.2	0.3	0.01	0.1	0.2	0.3
PPM	I	23.01	18.63	14.52	11.51	65.38	60.54	55.34	49.13	0.35	0.31	0.26	0.23
	II	0.00	1.92	3.56	4.11	0.23	2.31	4.57	7.84	0.00	0.83	0.78	0.52
	III	0.27	2.74	5.21	7.67	0.31	3.08	6.01	8.95	0.90	0.89	0.87	0.86
	IV	0.55	13.15	23.29	32.33	0.28	2.93	6.27	10.24	1.97	4.49	3.71	3.16
	V	76.16	63.56	53.42	44.38	33.80	31.15	27.81	23.84	2.25	2.04	1.92	1.86
PPM-CNN	I	1.92	2.47	0.27	3.01	7.59	5.01	7.71	6.30	0.25	0.49	0.04	0.48
	II	1.37	1.37	1.37	2.47	21.73	23.61	21.84	22.59	0.06	0.06	0.06	0.11
	III	5.75	6.85	5.48	5.48	29.61	31.69	28.58	32.77	0.19	0.22	0.19	0.17
	IV	44.66	50.14	38.90	50.68	25.18	25.25	27.18	24.65	1.77	1.99	1.43	2.06
	V	46.30	39.18	53.97	38.36	15.89	14.44	14.68	13.68	2.91	2.71	3.68	2.80

In addition, the landslide frequency ratio (FR) can be computed to reflect the LSM accuracy. For each susceptibility grade, FR is the ratio of the percentage of landslide inventory points falling into the graded area to the percentage of that graded area. As shown in Table 3, the highest percentage of landslides was observed in the very high landslide susceptibility level (V) by employing the PPM model. This result indicates that the PPM model presents superior accuracy in identifying very high-risk areas. However, as the COV increases, the FR of very high susceptibility

areas gradually decreases. This implies that the landslide risk predicted by the physical model tends to transfer to high susceptibility (IV) areas. In contrast, the PPM-CNN model shows little change in FR when used for landslide susceptibility mapping (LSM) in the extremely low susceptibility area. In regions with low and moderate susceptibility, FR initially increases rapidly and then gradually decreases; and in regions with high and very high susceptibility, the increase in frequency ratios is more pronounced. The results highlight that the PPM-CNN model can effectively capture spatial variability under different parameter uncertainties. Additionally, noted that the percentage of landslides increases significantly as susceptibility increases. This indicates that the model provides a more balanced assessment of landslide susceptibility assessments. The balance between accuracy and complexity in LSM may be attributed to its deep learning architecture for PPM-CNN, which enables the automatic identification and exploration of complex spatial patterns in the data.

4.3.2. Frequency distribution analysis of landslide susceptibility considering different *COV* scenarios

To comprehensively understand the differences in LSM obtained by PPM-CNN involving parameter uncertainties, the distributions of normalized susceptibility value (NSV) are introduced and compared under different *COV* conditions (ranging from 0.01 to 0.30) (Chang et al., 2022). As depicted in Fig. 12, the NSV distributions at *COV* values of 0.01, 0.10, 0.20, and 0.30 respectively, along with their corresponding mean and standard deviation (STD) values, provide crucial insights into the trend and degree of dispersion within NSV distribution. The mean values indicate the concentration trend of NSV, while the STD values reflect its level of dispersion. Fig. 12 shows that NSV distribution generally follows an approximately normal pattern under different *COV* conditions (red line). However, it can be observed that as *COV* increases, the degree of dispersion within NSV does not exhibit a linear variation by examining the developmental pattern of NSV distribution on the normal curve (red line). The distribution of NSV aligns most closely with the fitted normal distribution curve before gradually dispersing when *COV* = 0.2. This nonlinearity highlights the impact of *COV* on landslide susceptibility derived from the PPM-CNN method.

It is worth noting that most grid cells exhibit $NSV \approx 0.5$. This contrasts with the approach to landslide susceptibility assessment, whereby most grid cells exhibit relatively low landslide susceptibility, even in major mountainous regions. However, this discrepancy reflects the advantage of capturing the correlation of spatial data by using the proposed model. For instance, some recent studies (Wei et al., 2021; Liu et al., 2024) have demonstrated that the combination of a PPM with ML can effectively identify intricate patterns and features in the data, which may be challenging to discern using solely physical models. This is also evident in Fig. 11, which illustrates that the susceptibility areas identified through the PPM method are predominantly classified as either very low or very high. In contrast, the application of PPM-CNN tends to categorize most regions experiencing heavy rainfall (after 9 h) as moderate susceptibility areas. This indicates that, in addition to the areas where landslides have been documented to occur (which correspond to areas of high and very high susceptibility), attention should be paid to areas of moderate susceptibility areas. This is consistent with the observation that the area of slope instability in the region expands further following sustained rainfall as well (He et al., 2021; Cui et al., 2024).

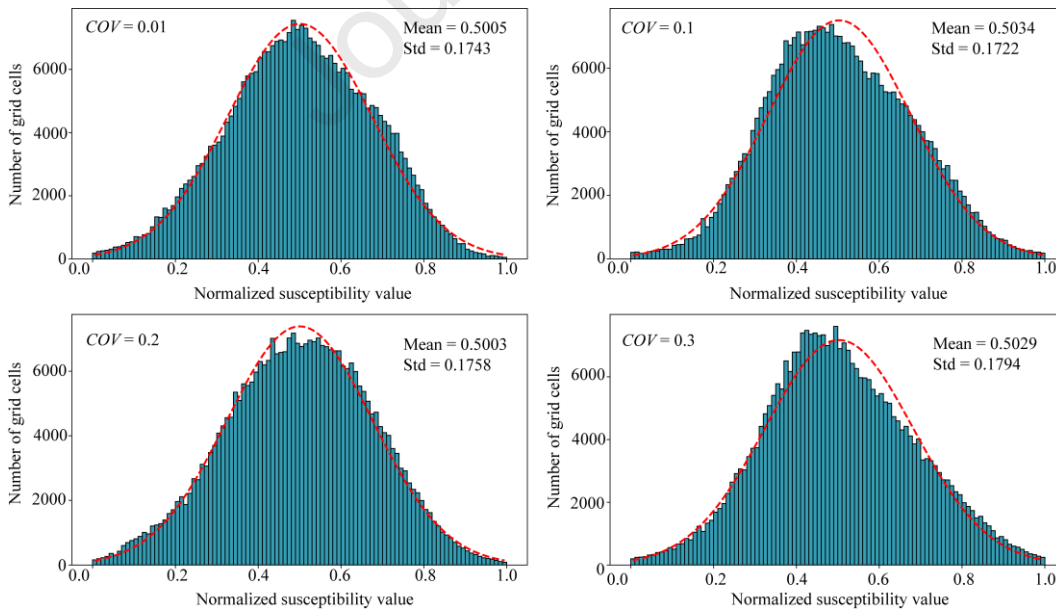


Fig. 12. Frequency distribution of normalized susceptibility value (NSV) under different *COV*s by adopting the PPM-CNN model: *COV* = (a) 0.01, (b) 0.10, (c) 0.20, and (d) 0.30.

As shown in Fig. 13a, the proportion of areas classified as 'high' and 'very high' susceptibility follows a trend of increasing and then decreasing as the *COV* values develop. For example, at *COV* = 0.01, approximately 15.9% of areas are classified as 'very high' susceptibility, while

this decreases to around 13.7% or 13.9% as the COV rises to 0.30. To illustrate the impact of various COVs on regional stability, a random sample of 1000 non-landslide points was selected from the study region. Fig. 13b and c presents the proportion of susceptibility grades of inventory points and random points. The proportion of inventory points in different susceptibility grades indicates a significant increase with higher susceptibility levels when $COV = 0.2$.

For the same COV, non-landslide (random) points exhibit the highest proportion within the high susceptibility grade area. In contrast, there are more random points located in the high susceptibility area at lower and higher COV values (i.e. 0.1, 0.3). The phenomenon arises from the initial PPM prediction, which is grounded in physical laws and yields a feature space with significant physical implications for CNN. Subsequently, CNN engages in deep learning within this feature space to discern intricate patterns and correlations within the data. Therefore, the proposed model demonstrates enhanced sensitivity in recognizing features and capturing the impact of uncertainty in geotechnical parameters on the prediction of landslide susceptibility. Note that maintaining a moderate level of $COV = 0.2$ is crucial for accurate analysis. This combination provides a better balance between data uncertainty and model prediction capability, which results in optimal predictive performance and effective differentiation of landslide points at different susceptibility levels. High COV values can cause uncertainty that exceeds the ability of the model to optimize the identification of key features. This may cause a blurred distribution of landslide and non-landslide points within the susceptibility class, which could result in overfitting or an exaggerated response to abnormal values.

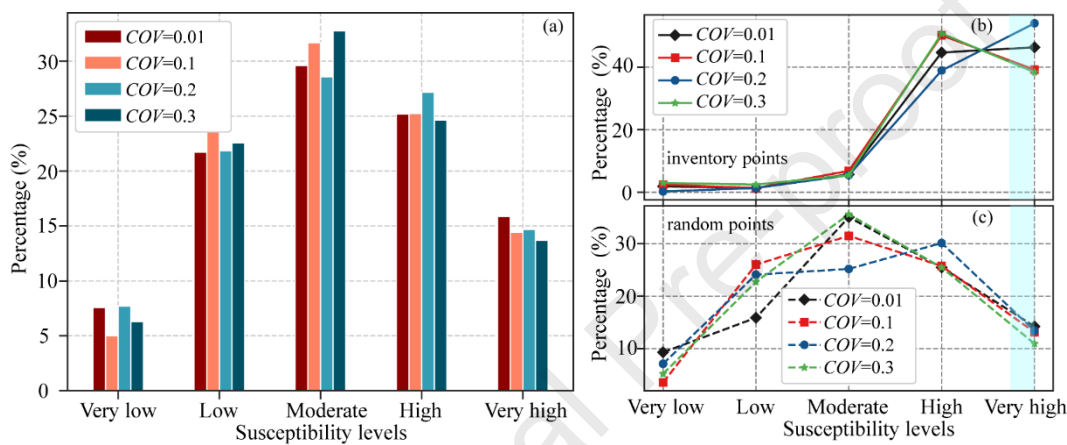


Fig. 13. Quantitative analysis of landslide susceptibility distribution under different COVs.

4.3.3. Statistical analysis of the results under different COV scenarios

For facilitating further analysis of results under different COV scenarios, the ternary diagram is introduced in these conditioning factors of landslide susceptibility which widely employed in fields such as chemistry, metallurgy, and geology (Giannetti et al., 2006; Hamilton and Ferry, 2018). This application aids in identifying and evaluating interactions between identifying evaluating interactions between influence factors as well as between landslides and external topographic elements. Therefore, the slope and aspect were considered as typical factors.

Fig. 14 illustrates the statistical distribution of slope and aspect for inventory and random points under different COV scenarios. As shown in Fig. 14a and b, the ternary phase diagrams indicate that areas with higher terrain slopes and aspects have lower landslide susceptibility levels for both inventory and random points and vice versa. Additionally, the higher COV indicates a more significant clustering effect which suggests that landslide risk is elevated in areas with low slope and high COV. Due to the gentle slope and dense vegetation, the soil saturates quickly during rainfall, which increases the potential for landslides. On the other hand, the aspect does not significantly influence landslide susceptibility compared to terrain slopes. Fig. 14c illustrates a moderate increase in the mean slope and its 95% confidence interval for inventory points located in areas of very high susceptibility as COV increases. This implies that very high susceptibility areas are inclined to develop on terrain with steeper slopes. The distribution of slopes for random points (see Fig. 14e) shows a general decrease in the mean slope and its 95% points in non-landslide areas as COV values increase. This indicates that the potential of landslides occurring on lower slopes is higher under conditions of increased uncertainty in geotechnical parameters. Furthermore, the radar plots (Fig. 14d and f) indicate an increase in landslide susceptibility on slopes facing north and northeast when geotechnical parameters are uncertain. This emphasizes the significance of the north-facing and northeast-facing aspects in predicting landslides.

4.4. Influence of cross-correlation and statistical distribution of random variables

Accurate landslide susceptibility assessment based on probability analysis necessitates the consideration of interdependencies among potential physical parameters. The multiple random variables such as terrain elevation, rainfall, and soil type may affect POF, especially for

parameters like soil cohesion (c) and friction angle (ϕ) that do not follow a normal distribution. Hence, it is imperative to simultaneously consider correlation and non-normal distribution in determining POF. To achieve this, the preferred approach involves the utilization of the lognormal distribution for replicating the probability distributions of parameters c and ϕ , as suggested by Ji et al. (2015). The remaining parameters are assumed to be deterministic which allows for the investigation of a negative correlation between c and ϕ without consideration of other parameters. Additionally, the negative correlation coefficient is assigned as -0.3.

4.4.1. Comparison between different scenarios of cross-correlation and statistical distribution

To investigate the influence of cross-correlation and statistical distribution of geotechnical parameters, the prediction of LSMs was conducted by applying the PPM and PPM-CNN models in this study area, respectively. As shown in Fig. 15a-d, most of the study area exhibits “very low” landslide susceptibility based on the LSMs calculated by the PPM, while the “high to very high” susceptibility areas are concentrated near the landslide inventory points. However, these areas identified in “very low” susceptibility using PPM are reclassified as “low and mediate” susceptibility by employing the PPM-CNN model (Fig. 15e-h). Note that some inventory landslides that were originally reclassified in areas of very high susceptibility when adopting PPM were observed to be in the areas of high susceptibility.

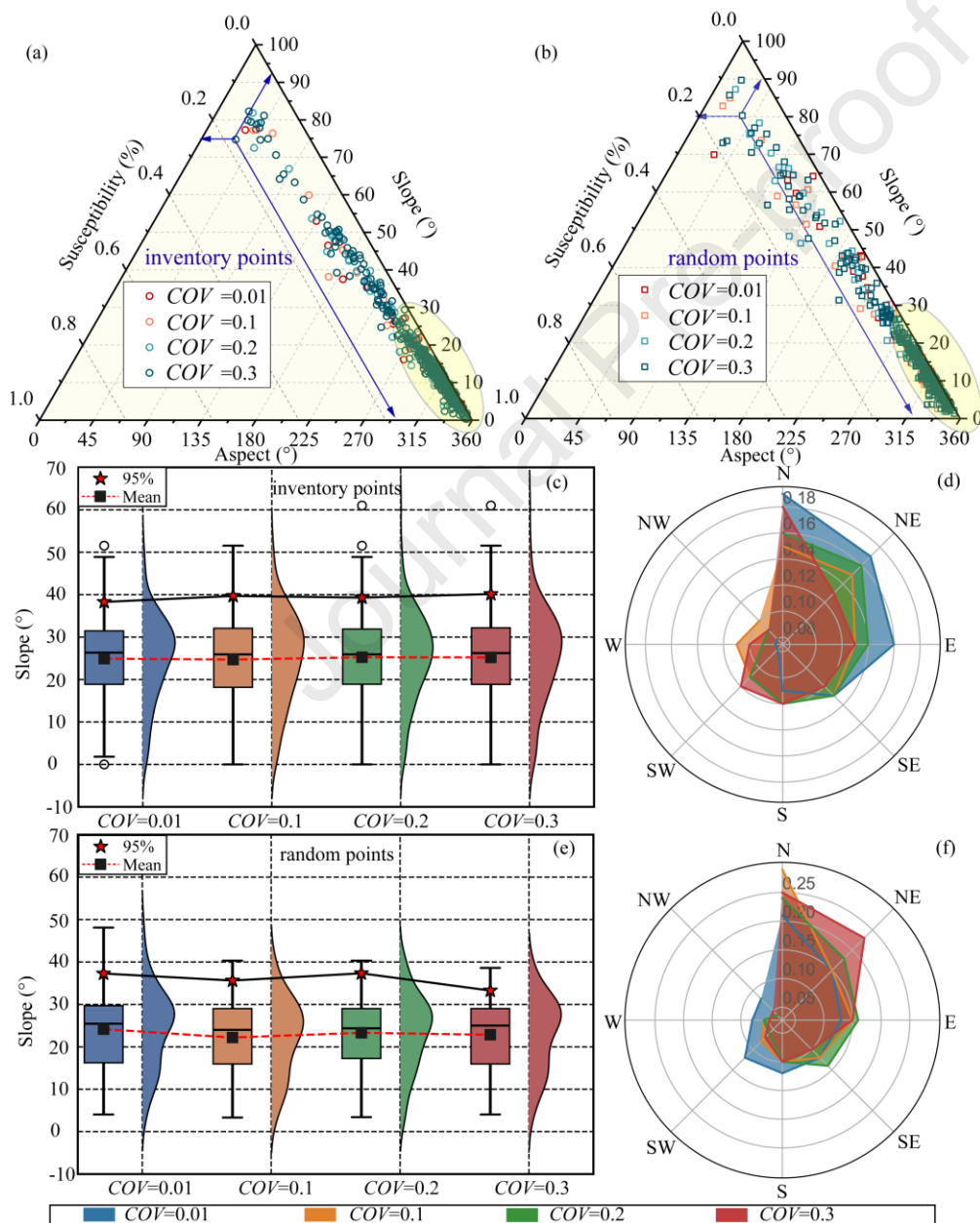


Fig. 14. Results of slope angles and aspects for very high susceptibility areas considering different COV conditions: ternary phase diagram (a) inventory points, (b) random points; very high susceptibility areas under different COV scenarios of box-dumbbell schematic: (c) inventory points, (e) random points; very high susceptibility areas along with aspect: (d) inventory points, (f) random points.

The LSMs of cross-correlation and the statistical distribution of random variables indicate that 76.16% inventory points are in areas with high susceptibility when using the PPM model (as listed in Table 4). However, only 63.56% inventory landslides were classified as very high susceptibility areas after considering the cross-correlation of parameters. This implies that the statistical correlation of parameters results in a higher prevalence of high-susceptibility areas, irrespective of whether the distribution is normal or non-normal. Furthermore, the magnitude of FR values in high and very high susceptibility areas exhibited a substantial increase, reaching more than ten times higher than those observed in areas with very low susceptibility.

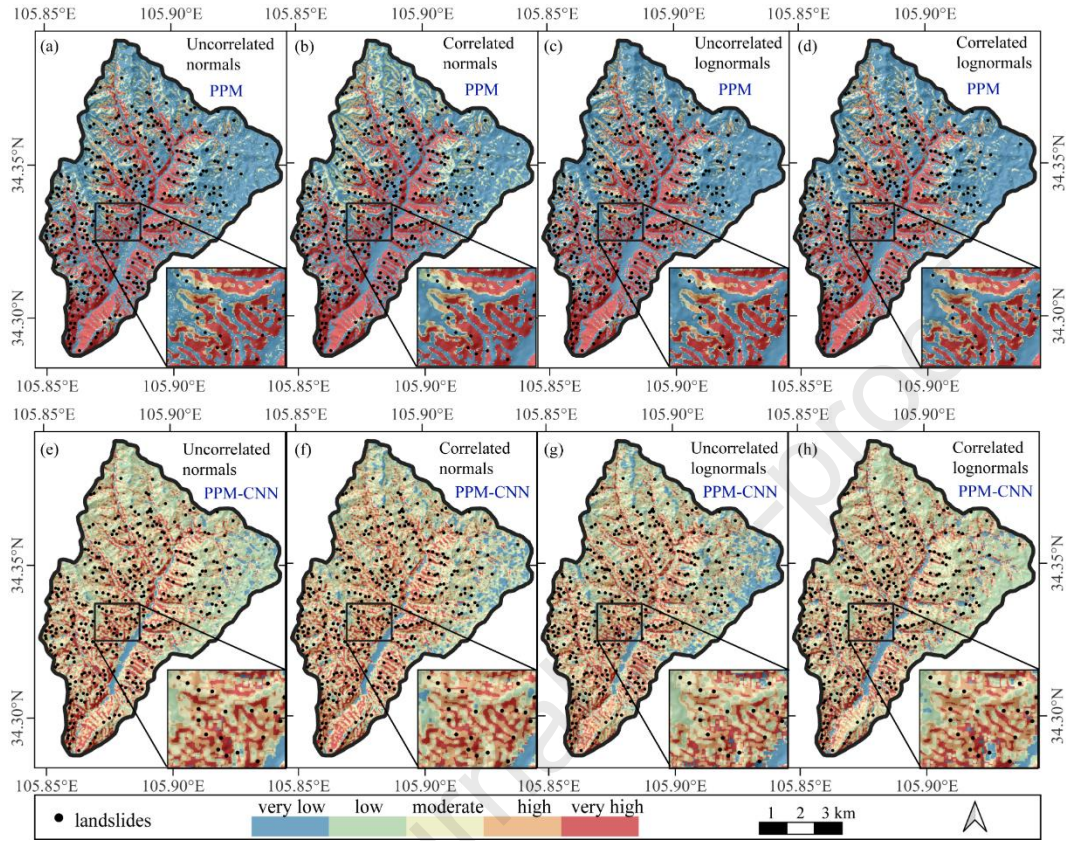


Fig. 15. Landslide susceptible distribution under different cross-correlation and statistical distributions.

Table 4

FR among the landslide susceptibility classes for different cross-correlation and statistical distribution.

Method	Susceptibility grade	Percentage of landslide numbers (%)				Percentage of graded area (%)				Frequency ratio			
		UN	CN	UL	CL	UN	CN	UL	CL	UN	CN	UL	CL
PPM	I	23.01	18.63	14.52	11.51	65.38	60.54	55.34	49.13	0.35	0.31	0.26	0.23
	II	0.00	1.92	3.56	4.11	0.23	2.31	4.57	7.84	0.00	0.83	0.78	0.52
	III	0.27	2.74	5.21	7.67	0.31	3.08	6.01	8.95	0.90	0.89	0.87	0.86
	IV	0.55	13.15	23.29	32.33	0.28	2.93	6.27	10.24	1.97	4.49	3.71	3.16
	V	76.16	63.56	53.42	44.38	33.80	31.15	27.81	23.84	2.25	2.04	1.92	1.86
PPM-CNN	I	2.47	1.10	5.75	3.29	5.01	7.87	5.74	9.66	0.49	0.14	1.00	0.34
	II	1.37	3.01	2.47	1.37	23.61	20.07	26.40	21.32	0.06	0.15	0.09	0.06
	III	6.85	4.11	14.79	9.32	31.69	29.09	30.58	30.27	0.22	0.14	0.48	0.31
	IV	50.14	50.14	48.22	53.97	25.25	28.82	25.08	26.05	1.99	1.74	1.92	2.07
	V	39.18	41.64	28.77	32.05	14.44	14.14	12.20	12.70	2.71	2.94	2.36	2.52

Note: UN: uncorrelated normals; CN: correlated normals; UL: uncorrelated lognormals; CL: correlated lognormals

4.4.2. Frequency distribution of landslide susceptibility considering cross-correlation and statistical distribution in random variables

To further analyze the influence of cross-correlation and statistical distribution for landslide susceptibility, the frequency distribution is adopted by combining NSV. Fig. 16 illustrates that considering correlation leads to a slightly more dispersed distribution of sensitivity values

compared to assuming no correlation in both 'normal uncorrelated' and 'normal correlated' cases. This suggests that parameter correlation may result in more localized variability in landslide susceptibility. However, both the 'lognormal uncorrelated' and 'lognormal correlated' models exhibit a long-tailed nature, as evidenced by a more concentrated peak with significant long tails when considering non-normal parameters. This also confirms that non-normal parameter distributions play a significant role in affecting spatial landslide susceptibility.

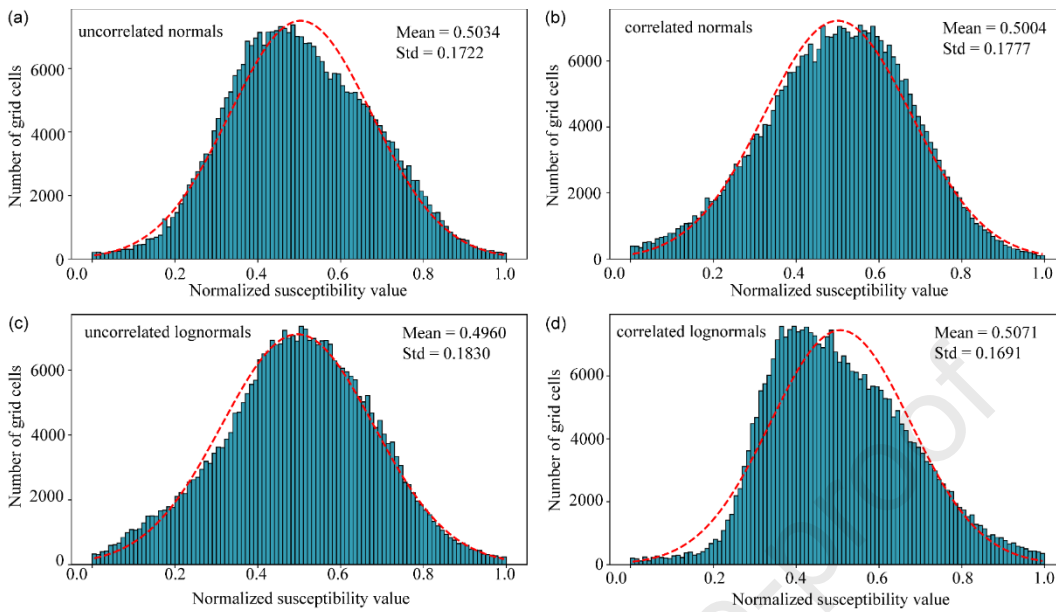


Fig. 16. Frequency distribution of normalized susceptibility value under different cross-correlation and statistical distribution by adopting PPM-CNN model.

In addition, the proportion of unstable regions categorized as 'high' and 'very high' decreases when the parameters conform to a lognormal distribution compared to a normal distribution as shown in Fig. 17a. For instance, in the lognormal uncorrelated condition, unstable regions accounted for 38.8% of the total study area compared to 39.7% in the normal uncorrelated condition. Moreover, both lognormal and standard normal distributions showed lower percentages of very high susceptibility regions when considering correlation than when not considering it. This indicates that the inclusion of parameter correlation and non-normal distributions is effective in reducing false positives.

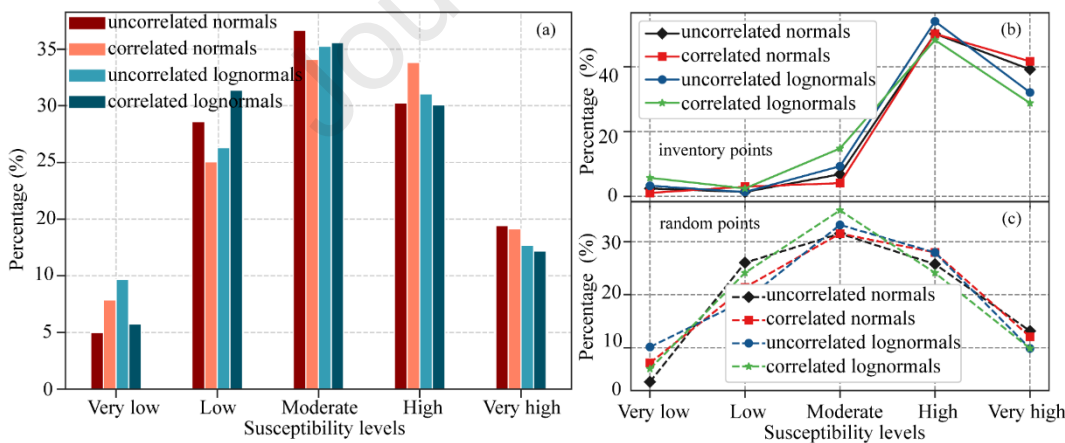


Fig. 17. Quantitative analysis of landslide susceptibility distribution under different cross-correlation and statistical distribution.

4.4.3. Statistical analysis of the results considering parameters cross-correlation and statistical distribution

To further investigate the influence of typical terrain factors (terrain slope and aspect) on landslide susceptibility mapping, statistical analyses including ternary phase diagrams, box plots and radar plots were conducted for both inventory points and random points, as shown in Fig. 18. The results of ternary phase diagrams indicate that high susceptibility areas, both in the inventory and random points, are concentrated in regions with lower terrain slopes and greater aspects (Fig. 18a and b), which is also reflected in Section 4.3.3. However, the level of landslide susceptibility was higher in the case of low slopes with high slope orientation and the presence of correlation between geotechnical parameters after analyzing the clustering effect of the inventory and random points. Fig. 18c and e illustrates the slope distributions of inventory points and random points, respectively. The slope distributions of inventory landslide points exhibited higher values across all parameter conditions

compared to random points which is particularly evident under the lognormal correlation condition. Notably, a narrower interquartile range suggests that capturing the effect of topography on landslide susceptibility becomes more accurate with correlated parameters when considering parameter correlations (correlated normals (CN) and correlated lognormals (CL)). Note that the landslide susceptibility distribution along different aspects as shown in radar plots (Fig. 18d and f). The inventory points of aspect are primarily concentrated in the north-facing to north-east-facing regardless of cross-correlation or non-normal for geotechnical parameters. This further implies that slopes facing north and northeast should be focused on involving the landslide prediction for Niangniangba areas.

4.5. Limitations and recommendations

In this study, a novel framework combines the PPM-CNN for evaluating landslide susceptibility at the regional scale. In contrast to the conventional approach to selecting non-landslide samples, the method proposed here is based on the probabilistic physical model of PRL-STIM. This allows for a comprehensive consideration of the physical-mechanical mechanisms of rainfall-induced landslides, as well as the inherent uncertainty associated with the geotechnical parameters. This approach effectively excludes unsuitable non-landslide samples. Furthermore, this method can also mitigate the issue of data noise and reduce the risk of overfitting the model during the training process. Furthermore, the mapping accuracy (AUC) is also significantly improved by employing OpenCV. An actual example of a rainfall-induced shallow landslide in Niangniangba Town, Gansu Province, China, was selected to verify the performance of the proposed approach. However, the challenges and limitations of assessing landslide susceptibility are undeniable as follows:

- (1) One of the main limitations of this study is the quality of the input data, a common issue that has been discussed by numerous researchers (Tran et al., 2018; Yi et al., 2020; Cui et al., 2024; Li et al., 2024). In this study, we have simply adapted the source data provided in the literature. Considering data availability and ease of processing, spatial resolutions of input raster files were standardized to 12.5 m. Indeed, from a physical modeling perspective, the 12.5m resolution provides limited spatial information on landslide geometry compared to higher resolutions. However, it is important to note that higher resolution of DEM does not necessarily result in improved predictions of landslide susceptibility (Bueechi et al., 2019; Chen et al., 2020). Therefore, a trade-off between raster data resolution and model performance is necessary for different regions.
- (2) The incorporation of landslide susceptibility in this study does not directly consider the conditional probabilities of past landslides. Instead, the presented failure probabilities are derived from a combination of physical modeling and probabilistic analytical techniques. Specifically, the assessment of the correlation between landslide occurrence and influence factors can entail the consideration of combinations of different data layers, heterogeneity of input data, and uncertainty (Wang et al., 2020). This is typically addressed through the certainty factor (CF) method. Nevertheless, this aspect is not investigated in the current study, precluding the consideration of conditional probabilities associated with identified landslides.
- (3) Regarding the applicability for different magnitudes of rainfall events in new areas, the methodology presented significant portability by integrating the PRL-STIM physical model with CNN. In the case of a new area, the specific physical parameters of the area can be input into the physical model with full consideration of the corresponding rainfall intensity when confronted with rainfall events of varying magnitudes. This allows for the calculation of different failure probability distribution maps. In essence, the method proposed in this work is founded upon a physical model, which enables the incorporation of the most recent landslide events and physical parameter information. This, in turn, facilitates the dynamic adjustment of the model results, thereby enhancing the accuracy of the prediction. Although geological conditions and rainfall patterns may vary from one region to another, the methodology proposed in this paper can perform effective landslide susceptibility analysis for new regions, considering local geological formations, vegetation cover and rainfall characteristics. This methodology exhibits greater generalization ability and higher robustness, which not only enhances the prediction of landslide risk but also provides a scientific foundation for disaster mitigation and prevention.

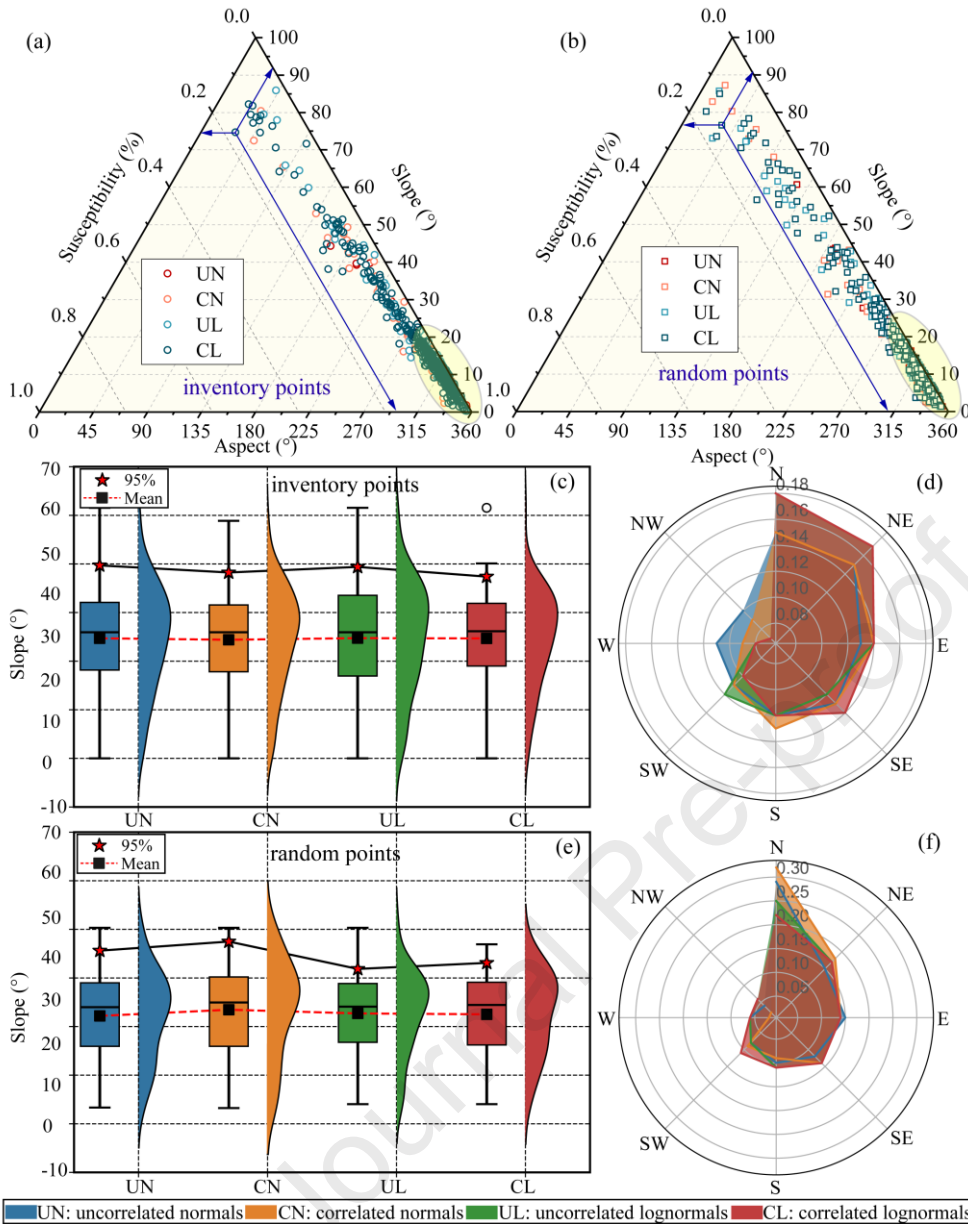


Fig. 18. Results of slope angles and aspects for susceptibility areas considering cross-correlation and statistical distribution: Ternary phase diagram (a) inventory points, (b) random points; very high susceptibility areas under cross-correlation and statistical distribution scenarios of box-dumbbell schematic: (c) inventory points, (e) random points; very high susceptibility areas along with aspect: (d) inventory points, (f) random points.

5. Conclusions

In this study, a novel framework for assessing regional landslide susceptibility was proposed which is referred to as "physically-based probabilistic modeling fusion convolutional neural network (PPM-CNN)". The approach combines the proposed PRL-STIM with the widely adopted CNN deep learning model to enhance the probability assessment of rainfall-induced shallow landslides at the regional scale. The main results are as follows:

- (1) The PPM-CNN model effectively integrates the physically-based probabilistic modeling of landslides with CNN deep learning. This enhances both interpretability and generality through a data-driven approach that combines physical mechanics methods and engineering reliability analysis. Furthermore, this addresses the challenge of limited generalization ability in the regions with uncertainties of geotechnical parameters applications commonly related to CNNs.
- (2) The hybrid PPM-CNN model effectively captures both spatial and channel correlations among different state factors. The PRL-STIM model serves as an information amplifier, enhancing the accuracy of landslide probability predictions. Incorporating various

probability parameter information for sample pre-selection significantly enhances the predictive capability and robustness of the CNN in scenarios with limited input data. The prediction accuracy reaches an impressive 85%, representing a substantial improvement over the AUC values obtained from a standalone CNN model.

- (3) The spatial distribution of unstable regions is significantly influenced by the uncertainty associated with physical parameters at the regional scale. The dispersion of unstable regions becomes more pronounced as the *COV* increases. Additionally, cross-negative correlation with unnormal parameters impacts the proportion of highly and moderately susceptible areas.

Declaration of Competing Interest

The authors declare that they have no known competing financial interests or personal relationships that could have appeared to influence the work reported in this paper.

Acknowledgements

We acknowledge the funding support from the National Natural Science Foundation of China (Grant Nos: U22A20594, 52079045). Hongzhi Cui acknowledges the financial support of the China Scholarship Council (Grant No. CSC: 202206710014) for his research at Universitat Politècnica de Catalunya, Barcelona.

References

- Anantrasirichai, N., Biggs, J., Albino, F., Bull, D., 2019. The Application of Convolutional Neural Networks to Detect Slow, Sustained Deformation in InSAR Time Series. *Geophys. Res. Lett.* 46(21), 11850–11858.
- Balogun, A.L., Rezaie, F., Pham, Q.B., Gigović, L., Drobniak, S., Aina, Y.A., Panahi, M., Yekeen, S.T., Lee, S., 2021. Spatial prediction of landslide susceptibility in western Serbia using hybrid support vector regression (SVR) with GWO, BAT and COA algorithms. *Geosci. Front.* 12(3), 1–15.
- Baum, R.L., Savage, W.Z., Godt, J.W., 2008. TRIGRS: a Fortran program for transient rainfall infiltration and grid-based regional slope-stability analysis, version 2.0. US Geological Survey, Reston, Virginia, USA.
- Bueechi, E., Klimeš, J., Frey, H., Huggel, C., Strozzi, T., Cochachin, A., 2019. Regional-scale landslide susceptibility modelling in the Cordillera Blanca, Peru—a comparison of different approaches. *Landslides.* 16(2), 395–407.
- Catani, F., Segoni, S., Falorni, G., 2010. An empirical geomorphology-based approach to the spatial prediction of soil thickness at catchment scale. *Water Resour. Res.* 46(5), 1–15.
- Chang, Z.L., Catani, F., Huang, F.M., Liu, G.Z., Meena, S.R., Huang, J.S., Zhou, C.B., 2022. Landslide susceptibility prediction using slope unit-based machine learning models considering the heterogeneity of conditioning factors. *J. Rock Mech. Geotech. Eng.* 15(5), 1127–1143.
- Chen, Z., Song, D., Dong, L., 2023. An innovative method for landslide susceptibility mapping supported by fractal theory, GeoDetector, and random forest: a case study in Sichuan Province, SW China. *Nat. Hazards.* 118(3), 2543–2568.
- Chen, Z., Ye, F., Fu, W.X., Ke, Y.T., Hong, H.Y., 2020. The influence of DEM spatial resolution on landslide susceptibility mapping in the Baxie River basin, NW China. *Nat. Hazards.* 101(3), 853–877.
- Cui, H.Z., Hürlimann, M., Medina, V., Ji, J., 2023. GIS-FSLAM-FORM: A QGIS plugin for fast probabilistic susceptibility assessment of rainfall-induced landslides at regional scale. Presented at the EGU23 General Assembly, Copernicus Meetings, Vienna, Austria.
- Cui, H.Z., Ji, J., Hürlimann, M., Medina, V., 2024. Probabilistic and physically-based modelling of rainfall-induced landslide susceptibility using integrated GIS-FORM algorithm. *Landslides.* 6(21), 1461–1481.
- Cui, H.Z., Ji, J., Song, J., Huang, W.G., 2022. Limit state line-based seismic stability charts for homogeneous earth slopes. *Comput. Geotech.* 146, 104749.
- Fang, Z.C., Wang, Y., Duan, H.X., Niu, R.Q., Peng, L., 2022. Comparison of general kernel, multiple kernel, infinite ensemble and semi-supervised support vector machines for landslide susceptibility prediction. *Stoch. Environ. Res. Risk Assess.* 36(10), 3535–3556.
- Giannetti, B.F., Barrella, F.A., Almeida, C.M.V.B., 2006. A combined tool for environmental scientists and decision makers: Ternary diagrams and emergy accounting. *J. Clean. Prod.* 14(2), 201–210.
- Green, W.H., Ampt, G.A., 1911. Studies on Soil Physics. *J. Agric. Sci.* 4(1), 1–24.

- Hamilton, N.E., Ferry, M., 2018. ggtern: Ternary diagrams using ggplot2. *J. Stat. Softw.* 87(Code Snippet 3), 1–17.
- He, J.Y., Qiu, H.J., Qu, F., ang, Hu, S., Yang, D., Shen, Y.D., Zhang, Y., Sun, H.S., Cao, M.M., 2021. Prediction of spatiotemporal stability and rainfall threshold of shallow landslides using the TRIGRS and Scoops3D models. *Catena*. 197, 104999.
- Hess, D., Leshchinsky, B., Bunn, M., Mason, B.H., Olsen, M.J., 2017. A simplified three-dimensional shallow landslide susceptibility framework considering topography and seismicity. *Landslides*. 14(5), 1677–1697.
- Hong, H.Y., Miao, Y.M., Liu, J.Z., Zhu, A.X., 2019. Exploring the effects of the design and quantity of absence data on the performance of random forest-based landslide susceptibility mapping. *Catena*. 176, 45–64.
- Huang, F.M., Li, R.H., Catani, F., Zhou, X.T., Zeng, Z.Q., Huang, J.S., 2024. Uncertainties in landslide susceptibility prediction: Influence rule of different levels of errors in landslide spatial position. *J. Rock Mech. Geotech. Eng.* S1674775524000714.
- Huang, W.G., Loveridge, F., Satyanaga, A., 2022. Translational upper bound limit analysis of shallow landslides accounting for pore pressure effects. *Comput. Geotech.* 148, 104841.
- Hungr, O., Leroueil, S., Picarelli, L., 2014. The Varnes classification of landslide types, an update. *Landslides*. 11(2), 167–194.
- Hwang, I.T., Park, H.J., Lee, J.H., 2023. Probabilistic analysis of rainfall-induced shallow landslide susceptibility using a physically based model and the bootstrap method. *Landslides*. 20(4), 829–844.
- Ji, J., Cui, H., Zhang, T., Song, J., Gao, Y., 2022. A GIS-based tool for probabilistic physical modelling and prediction of landslides: GIS-FORM landslide susceptibility analysis in seismic areas. *Landslides*. 19(9), 1–19.
- Ji, J., Kodikara, J.K., 2015. Efficient reliability method for implicit limit state surface with correlated non-Gaussian variables. *Int. J. Numer. Anal. Methods Geomech.* 39(17), 1898–1911.
- Ji, J., Zhang, C.S., Gao, Y.F., Kodikara, J., 2019. Reliability-based design for geotechnical engineering: An inverse FORM approach for practice. *Comput. Geotech.* 111, 22–29.
- Kalantar, B., Pradhan, B., Naghibi, S.A., Motevalli, A., Mansor, S., 2018. Assessment of the effects of training data selection on the landslide susceptibility mapping: a comparison between support vector machine (SVM), logistic regression (LR) and artificial neural networks (ANN). *Geomat. Nat. Hazards Risk*. 9(1), 49–69.
- Kim, J.H., Lee, K.W., Jeong, S.S., Kim, G.S., 2014. GIS-based prediction method of landslide susceptibility using a rainfall infiltration-groundwater flow model. *Eng. Geol.* 182, 63–78.
- Lee, L.M., Gofar, N., Rahardjo, H., 2009. A simple model for preliminary evaluation of rainfall-induced slope instability. *Eng. Geol.* 108(3–4), 272–285.
- Lei, T., Zhang, Y.X., Lv, Z.Y., Li, S.Y., Liu, S.G., Nandi, A.K., 2019. Landslide Inventory Mapping From Bitemporal Images Using Deep Convolutional Neural Networks. *IEEE Geosci. Remote Sens. Lett.* 16(6), 982–986.
- Li, P.L., Wang, Y., Si, T.Z., Ullah, K., Han, W., Wang, L.Z., 2024. MFFSP: Multi-scale feature fusion scene parsing network for landslides detection based on high-resolution satellite images. *Eng. Appl. Artif. Intell.* 127, 107337.
- Li, W.J., Fang, Z.C., Wang, Y., 2022. Stacking ensemble of deep learning methods for landslide susceptibility mapping in the three gorges reservoir area, China. *Stoch. Environ. Res. Risk Assess.* 36(8), 2207–2228.
- Liao, Z.H., Hong, Y., Wang, J., Fukuoka, H., Sassa, K., Karnawati, D., Fathani, F., 2010. Prototyping an experimental early warning system for rainfall-induced landslides in Indonesia using satellite remote sensing and geospatial datasets. *Landslides*. 7(3), 317–324.
- Liu, S.L., Wang, L.Q., Zhang, W.G., Sun, W., Wang, Y.H., Liu, J.P., 2024. Physics-informed optimization for a data-driven approach in landslide susceptibility evaluation. *J. Rock Mech. Geotech. Eng.* S167477552400088X.
- Liu, X.F., Zhu, H.H., Wu, B., Li, J., Liu, T.X., Shi, B., 2023. Artificial intelligence-based fiber optic sensing for soil moisture measurement with different cover conditions. *Measurement*. 206, 112312.
- Liu, Z.Q., Gilbert, G., Cepeda, J.M., Lysdahl, A.O.K., Piciullo, L., Hefre, H., Lacasse, S., 2021. Modelling of shallow landslides with machine learning algorithms. *Geosci. Front.* 12(1), 385–393.
- Low, B.K., Tang, W.H., 2007. Efficient spreadsheet algorithm for first-order reliability method. *J. Eng. Mech.* 133(12), 1378–1387.
- Lumb, P., 1962. Effect of rain storms on slope stability. Local Property & Printing Company, Limited.
- Mangalathu, S., Hwang, S.H., Jeon, J.S., 2020. Failure mode and effects analysis of RC members based on machine-learning-based SHapley additive

- exPlanations (SHAP) approach. *Eng. Struct.* 219, 110927.
- Medina, V., Hürlimann, M., Guo, Z., Lloret, A., Vaunat, J., 2021. Fast physically-based model for rainfall-induced landslide susceptibility assessment at regional scale. *Catena*. 201, 105213.
- Merghadi, A., Yunus, A.P., Dou, J., Whiteley, J., ThaiPham, B., Bui, D.T., Avtar, R., Abderrahmane, B., 2020. Machine learning methods for landslide susceptibility studies: A comparative overview of algorithm performance. *Earth-Sci. Rev.* 207, 103225.
- Mondini, A., Guzzetti, F., Melillo, M., 2023. Deep learning forecast of rainfall-induced shallow landslides. *Nat Commun.* 14(1), 1–10.
- Montgomery, D.R., Dietrich, W.E., 1994. A physically based model for the topographic control on shallow landsliding. *Water Resour. Res.* 30(4), 1153–1171.
- Montrasio, L., Valentino, R., Losi, G.L., 2011. Towards a real-time susceptibility assessment of rainfall-induced shallow landslides on a regional scale. *Nat. Hazards Earth Syst. Sci.* 11(7), 1927–1947.
- Pack, R.T., Tarboton, D.G., Goodwin, C.N., 1998. The SINMAP approach to terrain stability mapping, in: *Engineering Geology and Natural Hazards*. Presented at the 8th Congress of the International Association of Engineering Geology, Vancouver, British Columbia, Canada.
- Rahardjo, H., Lim, T.T., Chang, M.F., Fredlund, D.G., 1995. Shear-strength characteristics of a residual soil. *Can. Geotech. J.* 32(1), 60–77.
- Raid, A.M., Khedr, W.M., El-dosuky, M.A., Aoud, M., 2014. Image Restoration Based on Morphological Operations. *Int. J. Comput. Sci. Eng. Inf. Technol.* 4(3), 9–21.
- Raimondi, L., Pepe, G., Firpo, M., Calcaterra, D., Cevasco, A., 2023. An open-source and QGIS-integrated physically based model for Spatial Prediction of Rainfall-Induced Shallow Landslides (SPRIn-SL). *Environ. Model. Softw.* 160, 1–18.
- Sameen, M.I., Pradhan, B., Lee, S., 2020. Application of convolutional neural networks featuring Bayesian optimization for landslide susceptibility assessment. *Catena*. 186, 1–13.
- Segoni, S., Rossi, G., Catani, F., 2012. Improving basin scale shallow landslide modelling using reliable soil thickness maps. *Nat. Hazards*. 61(1), 85–101.
- Silva, F., Lambe, T.W., Marr, W.A., 2008. Probability and risk of slope failure. *J. Geotech. Geoenvironmental Eng.* 134(12), 1691–1699.
- Sun, D.L., Wang, J., Wen, H.J., Ding, Y.K., Mi, C.L., 2024. Landslide susceptibility mapping (LSM) based on different boosting and hyperparameter optimization algorithms: A case of Wanzhou District, China. *J. Rock Mech. Geotech. Eng.* S1674775524000337.
- Sun, H.W., Wong, H.N., Ho, K.K.S., 1998. Analysis of infiltration in unsaturated ground. Presented at the Proceedings of the annual seminar on slope engineering in Hong Kong, Hong Kong, 101–109.
- Topaçlı, Z.K., Özcan, A.K., Gokceoglu, C., 2024. Performance Comparison of Landslide Susceptibility Maps Derived from Logistic Regression and Random Forest Models in the Bolaman Basin, Türkiye. *Nat. Hazards Rev.* 25(1), 04023054.
- Tran, T.V., Alvioli, M., Lee, G., An, H.U., 2018. Three-dimensional, time-dependent modeling of rainfall-induced landslides over a digital landscape: a case study. *Landslides*. 15(6), 1071–1084.
- Ullah, K., Wang, Y., Fang, Z., Wang, L., Rahman, M., 2022. Multi-hazard susceptibility mapping based on convolutional neural networks. *Geosci. Front.* 13(5), 101425.
- Wang, Y., Fang, Z.C., Hong, H.Y., 2019. Comparison of convolutional neural networks for landslide susceptibility mapping in Yanshan County, China. *Sci. Total Environ.* 666, 975–993.
- Wang, Y., Fang, Z.C., Wang, M., Peng, L., Hong, H.Y., 2020. Comparative study of landslide susceptibility mapping with different recurrent neural networks. *Comput. Geosci.* 138, 104445.
- Wang, Z.Z., 2022. Deep Learning for Geotechnical Reliability Analysis with Multiple Uncertainties. *J Geotech Geoenviron Eng.* 148(4), 06022001.
- Wang, Z.Z., Xiao, C., Goh, S.H., Deng, M., 2021. Metamodel-Based Reliability Analysis in Spatially Variable Soils Using Convolutional Neural Networks. *J. Geotech. Geoenvironmental Eng.* 147(3), 04021003.
- Wei, X., Zhang, L.L., Luo, J.Y., Liu, D.S., 2021. A hybrid framework integrating physical model and convolutional neural network for regional landslide susceptibility mapping. *Nat. Hazards*. 109(1), 471–497.
- Yang, L., Cui, Y.L., Xu, C., Ma, S.Y., 2024. Application of coupling physics-based model TRIGRS with random forest in rainfall-induced landslide-susceptibility assessment. *Landslides*. 1–15.
- Ye, X., Zhu, H., Wang, J., Zheng, W., Zhang, W., Schenato, L., Pasuto, A., Catani, F., 2024. Towards hydrometeorological thresholds of reservoir-

induced landslide from subsurface strain observations. *Sci. China Technol. Sci.* 67(6), 1907–1922.

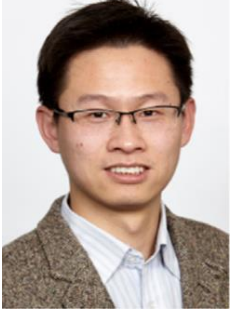
Yi, Y.N., Zhang, Z.J., Zhang, W.C., Jia, H.H., Zhang, J.Q., 2020. Landslide susceptibility mapping using multiscale sampling strategy and convolutional neural network: A case study in Jiuzhaigou region. *Catena*. 195, 104851.

Zeng, T.R., Jin, B.J., Glade, T., Xie, Y.Y., Li, Y., Zhu, Y.H., Yin, K.L., 2024. Assessing the imperative of conditioning factor grading in machine learning-based landslide susceptibility modeling: A critical inquiry. *Catena*. 236, 107732.

Zhang, H.Y., Li, C., Li, L., Cheng, S.Z., Wang, P., Sun, L.J., Huang, J.B., Zhang, X.Z., 2023. Uncovering the optimal structural characteristics of flocs for microalgae flotation using Python-OpenCV. *J. Clean. Prod.* 385, 135748.

Zhang, L.L., Zhang, J., Zhang, L.M., Tang, W.H., 2011. Stability analysis of rainfall-induced slope failure: a review. *Proc. Inst. Civ. Eng. - Geotech. Eng.* 164(5), 299–316.

Zhu, H.H., Ye, X., Pei, H.F., Zhang, W., Cheng, G., Li, Z.L., 2024. Probing multi-physical process and deformation mechanism of a large-scale landslide using integrated dual-source monitoring. *Geosci. Front.* 15(2), 101773.

	<p>Hongzhi Cui is currently a Ph.D. candidate in Geotechnical Engineering at Hohai University, China and UPC, Spain. He has been awarded a scholarship by the China Scholarship Council (CSC) to conduct research in the Division of Geotechnical Engineering and Geosciences, Department of Civil and Environmental Engineering, Universitat Politecnica de Catalunya, Spain from 2022 onwards. His research interests include (1) failure mechanism analysis of landslide hazards, (2) slope stability and reliability analysis, (3) landslide susceptibility assessment at the regional scale, and (4) machine learning in geotechnical engineering.</p>
	<p>Dr. Jian Ji is Professor in Geotechnical Engineering at Hohai University, China. He earned Ph.D. from the Nanyang Technological University (NTU), Singapore in 2012. His research interests include numerical analysis of geotechnical problems with probabilistic considerations, slope stability and landslide mitigation, and underground space safety and earth retaining systems. He received the 2018 Outstanding Paper Award and 2022 Scott Sloan Best Paper Award from <i>Computers and Geotechnics</i>. Dr. Ji is an Associate Editor of the journal <i>Advances in Civil Engineering</i>, editorial board member of international journals, such as <i>Computers and Geotechnics</i>, and <i>Marine Georesources & Geotechnology</i>. He is an elected ASCE Member and technical committee member of ISSMGE-TC201&TC304, ASCE-EDS. He serves as director of the Geotechnical Research Institute of Hohai University.</p>

Declaration of interests

The authors declare that they have no known competing financial interests or personal relationships that could have appeared to influence the work reported in this paper.

The authors declare the following financial interests/personal relationships which may be considered as potential competing interests:

Journal Pre-proof